

https://dspace.org/

The MeerKAT Massive Distant Clusters Survey detection of diffuse radio emission in galaxy clusters at z 1

Dakalo Phuravhathu; Matthew Hilton; SP Sikhosana; YC Perrott; T Mroczkowski ...

OXFORD UNIV PRESS
https://hdl.handle.net/10539/47305
WOS

Downloaded from a DSpace repository. https://dspace.org/

Monthly Notices of the ROYAL ASTRONOMICAL SOCIETY

MNRAS **542,** 1544–1561 (2025) https://doi.org/10.1093/mnras/staf1315
Advance Access publication 2025 August 11

The MeerKAT Massive Distant Clusters Survey: detection of diffuse radio emission in galaxy clusters at $z > 1$

Dakalo G. Phuravhathu [1]★ M. Hilton [1,2] S. P. Sikhosana [2,3] Y. C. Perrott [4] T. Mroczkowski,[5] L. Di Mascolo [6,7] D. Y. Klutse,[2,3] K. Knowles [3,8,9] J. van Marrewijk [10] K. Moodley,[2,3] B. Partridge,[11] C. Sifón [12] U. Sureshkumar [1] and E. J. Wollack [13]

[1]*Wits Centre for Astrophysics, School of Physics, University of the Witwatersrand, Private Bag 3, Johannesburg 2050, South Africa*
[2]*School of Mathematics, Statistics & Computer Science, University of KwaZulu-Natal, Westville Campus, Durban 4041, South Africa*
[3]*Astrophysics Research Centre, University of KwaZulu-Natal, Durban 3696, South Africa*
[4]*School of Chemical and Physical Sciences, Victoria University of Wellington, PO Box 600, Wellington 6140, New Zealand*
[5]*European Southern Observatory, Karl-Schwarzschild-Str 2, D-85748 Garching, Germany*
[6]*Kapteyn Astronomical Institute, University of Groningen, Landleven 12, NL-9747 AD Groningen, the Netherlands*
[7]*Université Côte d'Azur, Observatoire de la Côte d'Azur, CNRS, Laboratoire Lagrange , Nice, F-06304, France*
[8]*Centre for Radio Astronomy Techniques and Technologies, Department of Physics and Electronics, Rhodes University, PO Box 94, Makhanda 6140, South Africa*
[9]*South African Radio Astronomy Observatory, 2 Fir Street, Black River Park, Observatory, Cape Town 7925, South Africa*
[10]*Leiden Observatory, Leiden University, PO Box 9513, NL-2300 RA Leiden, the Netherlands*
[11]*Department of Astronomy, Haverford College, Haverford, PA 19041, USA*
[12]*Instituto de Física, Pontificia Universidad Católica de Valparaíso, Casilla 4059, Valparaíso, Chile*
[13]*NASA Goddard Space Flight Center, 8800 Greenbelt Rd, Greenbelt, MD 20771, USA*

Accepted 2025 August 8. Received 2025 July 29; in original form 2025 June 5

ABSTRACT

Diffuse, low surface brightness radio emission in merging galaxy clusters provides insights into cosmic structure formation, the growth of magnetic fields, and turbulence. This paper reports a search for diffuse radio emission in a pilot sample of six high-redshift ($1.01 < z < 1.31$) galaxy clusters from the MeerKAT Massive Distant Clusters Survey (MMDCS). These six clusters are selected as the most massive ($M_{500c} = 6.7$–$8.5 \times 10^{14}\,M_{\odot}$) systems based on their Sunyaev–Zel'dovich mass from the full MMDCS sample of 30 Atacama Cosmology Telescope Data Release 5 clusters, and were observed first to explore the high-mass, high-redshift regime. Diffuse radio emission is confidently detected in four clusters and tentatively identified in two, with k-corrected radio powers scaled to 1.4 GHz ranging from (0.46 ± 0.16) to $(4.51 \pm 1.68) \times 10^{24}\,\mathrm{WHz}^{-1}$ and linear sizes between 0.47 and 1.08 Mpc. Combining *Chandra* X-ray data with MeerKAT radio data, we find that 80 per cent of clusters with X-ray observations exhibit disturbed morphologies indicative of mergers. These $z > 1$ galaxy clusters scatter around the established radio power–mass scaling relation observed at lower redshifts, supporting turbulent reacceleration models in high-redshift mergers. However, their radio spectra are predicted to steepen ($\alpha < -1.5$) due to enhanced inverse Compton losses in the cosmic microwave background, rendering them underluminous at 1.4 GHz and placing them below the correlation. Our results demonstrate that merger-driven turbulence can sustain radio haloes even at $z > 1$ while highlighting MeerKAT's unique ability to probe non-thermal processes in the early Universe.

Key words: galaxies: clusters: general – galaxies: clusters: intracluster medium – radio continuum: general – X-rays: galaxies: clusters.

1 INTRODUCTION

Galaxy clusters, the largest gravitationally bound structures in the universe, form at the intersections of cosmic web filaments through a hierarchical process involving gravitational infall and mergers with smaller subclusters. These merger events, among the most energetic phenomena since the big bang, release tremendous energy ($\sim 10^{64}$ erg), a significant portion of which dissipates as shocks and turbulence within the intracluster medium (ICM; Sarazin 2002, 2003; Markevitch & Vikhlinin 2007). The turbulent activity heats the ICM to temperatures of 10^7–10^8 K, amplifies magnetic fields, and (re)accelerates cosmic ray electrons (CRe) to relativistic energies. These processes result in the emission of diffuse synchrotron radiation, observed as radio haloes and relics, which stem from the ICM rather than individual galaxies. However, it is important to note that while this mechanism is generally preferred, alternative models, such as hadronic processes, have been proposed

★ E-mail: dakalophuravha2@gmail.com

© The Author(s) 2025.
Published by Oxford University Press on behalf of Royal Astronomical Society. This is an Open Access article distributed under the terms of the Creative Commons Attribution License (https://creativecommons.org/licenses/by/4.0/), which permits unrestricted reuse, distribution, and reproduction in any medium, provided the original work is properly cited.

Downloaded from https://academic.oup.com/mnras/article/542/2/1544/8230804 by Witwatersrand University user on 14 October 2025

and are still actively debated (see review by Brunetti & Jones 2014).

Radio haloes and relics are large-scale radio sources (∼0.1–1 Mpc) that emit steep-spectrum radiation ($-1.0 \gtrsim \alpha \gtrsim -1.4$)[1] with very low surface brightness (∼μJy arcsec^{-2}; Macario et al. 2013; van Weeren et al. 2019; Parekh et al. 2020). However, they differ in terms of their location, morphology, and polarization properties. Radio haloes are centrally located within clusters and often trace the X-ray-emitting ICM, with a regular morphology and low polarization. The formation of radio haloes is primarily attributed to the reacceleration of pre-existing electrons due to turbulence within the ICM during cluster mergers, with the reacceleration process facilitated by magnetohydrodynamic (MHD) turbulence (Brunetti et al. 2001; Cassano & Brunetti 2005). Radio haloes have been found predominantly in merging clusters and show a close correlation with the X-ray emission from the ICM, further supporting the idea that their origin is tied to the thermal and non-thermal components of the cluster's central ICM (Cassano et al. 2010; Brunetti & Jones 2014).

In contrast, radio relics are located at the peripheral regions of galaxy clusters, often appearing as elongated, arc-shaped structures with high polarization (up to 70 per cent). Their formation mechanism is thought to originate from shock waves propagating through the ICM during cluster mergers, which accelerate electrons to relativistic speeds via the diffusive shock acceleration (Ensslin et al. 1998). The shock fronts, which typically have a Mach number between 1 and 3, are not always strong enough to accelerate electrons from the thermal pool alone (van Weeren et al. 2017; Sarkar et al. 2024), and thus, pre-accelerated populations of electrons are considered essential for the formation of relics (Hoeft & Brüggen 2007; Di Gennaro et al. 2023). Observational evidence suggests that relics often occur in merging clusters with non-relaxed dynamics. Their morphology can sometimes resemble that of shock waves, supporting the theory that they trace the outer edges of cluster mergers (Botteon et al. 2016; Rajpurohit et al. 2020).

The morphology of both the X-ray emission from the ICM (Sarazin 1988; Böhringer et al. 2000) and the distribution of galaxies within clusters provides valuable insights into their dynamical state (Dressler 1980). Galaxy clusters can be broadly classified as either dynamically relaxed or disturbed, with the latter often indicative of ongoing or recent merger activity (Mann & Ebeling 2012; Yuan & Han 2020; Yuan, Han & Wen 2022). Dynamically disturbed clusters show irregular morphologies and substructure, and often exhibit multiple brightest cluster galaxies (BCGs), while relaxed clusters tend to have a smooth, symmetric X-ray appearance centred on a single BCG (Parekh et al. 2015; Yuan & Han 2020). However, mergers that occur along the line of sight are often difficult to identify in projected X-ray images because they may not produce clear asymmetries or substructure. Mergers play a crucial role in generating the turbulence necessary for (re)accelerating CRe and producing diffuse radio emission (Brunetti & Jones 2014; Weeren et al. 2019). Specifically, cluster mergers drive shocks and turbulence within the ICM that can amplify magnetic fields (Carilli & Taylor 2002) and accelerate particles (Petrosian & Bykov 2008). Therefore, understanding the dynamical state of galaxy clusters is essential for interpreting the origin and properties of observed radio haloes and relics. In this paper, we will consider the X-ray morphology (using archival *Chandra* X-ray data) of our cluster sample together with the detected diffuse radio emission to gain insights into the dynamical processes at play in these high-redshift systems, contributing to the broader understanding of the link between cluster mergers and radio halo formation.

Diffuse radio emission is difficult to observe at higher redshifts ($z > 1$) due to three key reasons: the increased energy density of the cosmic microwave background (CMB) leads to more rapid energy losses of CRe through inverse Compton (IC) scattering; redshift dimming reduces the surface brightness of the emission; and magnetic fields may not yet be strong enough to sustain bright radio haloes, further limiting synchrotron luminosity (Brunetti & Jones 2014; Di Gennaro et al. 2021). These effects are predicted to suppress the occurrence of diffuse radio emission in high-redshift clusters. At lower redshifts ($0.22 < z < 0.65$), Knowles et al. (2021) report a detection rate of ∼70 per cent, while Di Gennaro et al. (2021, 2025) report a decline in detection rates from ∼50 per cent at $0.6 < z < 0.9$ to ∼9 per cent at $0.78 \leq z \leq 1.5$. This redshift-dependent suppression aligns with the $(1+z)^4$ scaling of IC losses and lower cluster masses of high-z clusters (Brunetti & Jones 2014). Observational challenges have limited the number of known high-redshift haloes and relics, with only a few detections reported beyond $z > 0.8$. Notable examples include the radio halo in 'El Gordo' (ACT-CL J0102−4915; Lindner et al. 2014) at $z = 0.870$ and the $z = 1.23$ halo in ACT-CL J0329.2−2330 (Sikhosana et al. 2025), with the latter being a part of our sample. Recent studies continue to push these limits, with the detection of diffuse radio emission at $z > 1.3$ (Di Gennaro et al. 2025) and a candidate minihalo at $z = 1.71$ reported by Hlavacek-Larrondo et al. (2025).

Recent advancements in observational technology have allowed more effective studies of diffuse radio emission using next-generation Square Kilometre Array precursor telescopes such as MeerKAT (Jonas & MeerKAT Team 2016; Camilo et al. 2018), Low Frequency Array (van Haarlem et al. 2013), and Australian Square Kilometre Array Pathfinder (Johnston et al. 2007). MeerKAT stands out as the most sensitive instrument currently operational in the Southern hemisphere, comprising a total of 64 dishes situated in South Africa's Karoo region (Jonas & MeerKAT Team 2016; Camilo et al. 2018; Mauch et al. 2020). Its wide frequency coverage (*UHF*: 580–1015 MHz; *L*: 900–1670 MHz; and *S*: 1750–3500 MHz) enables spectral studies of diffuse emission both within individual bands (in-band studies) due to their wide bandwidths and across multiple bands for broader frequency coverage. Approximately three-quarters of its antennas are concentrated within a dense core spanning a radius of just 1 km, enhancing sensitivity to extended structures, while its outer antennas provide sufficient resolution for compact sources even at higher redshifts. This capability allows MeerKAT to effectively observe low surface brightness emission while resolving compact sources, thereby facilitating significant advancements in our understanding of diffuse emissions within galaxy clusters.

In this paper, we present the findings of a search for diffuse emission in an initial subsample of six clusters selected from the MeerKAT Massive Distant Clusters Survey (MMDCS). In Section 2, we describe the sample selection and outline our MeerKAT observations and data reduction. The MeerKAT results are presented in Section 3, followed by a discussion in Section 4, and a summary and conclusions in Section 5. Throughout this paper, R_{500c} is defined as the radius within which the mean mass density of the cluster is 500 times the critical density of the universe at the cluster's redshift. M_{500c} corresponds to the total mass (dark matter, gas, and galaxies) enclosed within R_{500c}. We adopt the standard ΛCDM (Λ cold dark matter) cosmology with $H_0 = 70\,\mathrm{km\,s^{-1}\,Mpc^{-1}}$, $\Omega_\mathrm{m} = 0.3$, and $\Omega_\Lambda = 0.7$.

[1] $S_\nu \propto \nu^\alpha$, where S_ν is the source flux density at frequency ν and α is the spectral index.

Downloaded from https://academic.oup.com/mnras/article/542/2/1544/8230804 by Witwatersrand University user on 14 October 2025

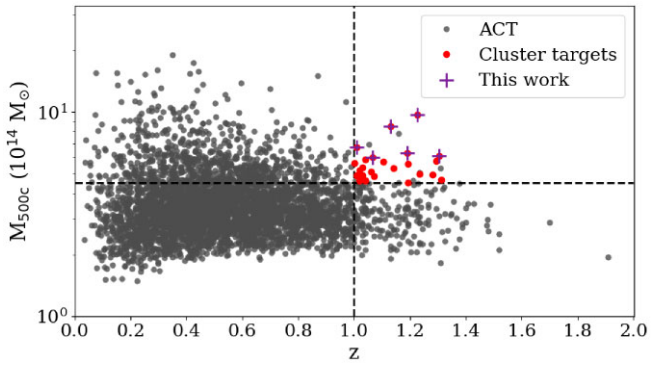

Figure 1. Mass versus redshift plot showing the ACT SZ-selected galaxy cluster catalogues (grey dots). The 30 MeerKAT target sample (red dots) are ACT clusters above $z > 1$ with mass (M_{500c}) $> 4.5 \times 10^{14}$ $M_\odot$, and within the DECaLS DR9 optical+IR survey (the dashed lines indicate the mass and z limits used; the six objects in the mass–z selection range that are not targeted are outside the DECaLS DR9 survey footprint). The purple crosses overlaid on six of these red dots indicate the specific clusters selected for this study.

2 OBSERVATIONS AND DATA REDUCTION

2.1 The cluster sample

The MMDCS is a MeerKAT L/UHF-band survey specifically designed to study a selection of 30 massive galaxy clusters at $z > 1$. The survey aims to study various aspects of these high-redshift clusters, including radio emission, star formation, active galactic nucleus (AGN) activity, and environmental effects within the cluster environments. The MMDCS sample comprises 30 of the most massive clusters selected from the Atacama Cosmology Telescope (ACT; Swetz et al. 2011) Data Release 5 (DR5) catalogue (Hilton et al. 2021). For this pilot study, we observed the six most massive clusters in the MMDCS sample (see Fig. 1). These clusters were prioritized to maximize sensitivity to diffuse emission in the high-mass regime, given the expected correlation between radio halo power and cluster mass (Cassano et al. 2013).

This catalogue contains over 4000 clusters, with 222 located at $z > 1$. The ACT catalogue is based on the Sunyaev–Zel'dovich (SZ) effect (Sunyaev & Zeldovich 1972), which is a powerful method for detecting galaxy clusters due to several unique properties: its redshift-independent surface brightness, the distinct spectral distortion of the CMB with a negative signal (decrement) at frequencies below 218 GHz, and the integrated flux density tracing thermal energy, which serves as a reliable proxy for total cluster mass. We restrict the selection to clusters with $z > 1$ and $M_{500cCal} > 4.5 \times 10^{14}$ $M_\odot$,[2] and which fall within the Dark Energy Camera Legacy Survey (DECaLS) Data Release 9 (DR9) optical+IR survey footprint (Dey et al. 2019), which provides essential data for source redshifts and classification (see Figs A1–A3). The target cluster sample covers redshift range $1.00 < z < 1.31$ and mass range $4.5 < M_{500c}/10^{14}$ $M_\odot < 9.7$ (see Fig. 1). The properties of the ACT SZ clusters are summarized in Table 1. In this study, we report on MeerKAT observations of a subsample comprising the six most massive clusters from the MMDCS sample. The full MMDCS sample will be analysed in future work.

[2] $M_{500cCal}$ refers to the richness-based, weak-lensing-calibrated mass estimate, which is considered the most accurate mass proxy available in ACT DR5 (Hilton et al. 2021).

2.2 Observation

The observations were conducted using the MeerKAT L-band receiver (PI: M. Hilton; proposal ID: SCI-20220822-MH-01), which operates between 856 and 1712 MHz, with a native bandwidth of 856 MHz and a central frequency of 1.28 GHz. The data were recorded using 4096 frequency channels and an integration time of 8 s per visibility, resulting in a total on-target time of 3.5 h per cluster, except for ACT-CL J2106.0−5844, which was observed for approximately 6 h. Primary calibrators were observed for 10 min at the start of each session for bandpass and flux calibration. Secondary calibrators were used for complex gain and delay calibration, alternating with target observations every 2 and 15 min, respectively. The details of the MeerKAT observations are summarized in Table 2.

2.3 Data reduction and imaging

We reduced the data using the OXKAT v0.4[3] software (Heywood 2020), a semi-automated tool designed for processing MeerKAT data. The OXKAT pipeline, consisting of PYTHON-based scripts, streamlines the data reduction process by incorporating various radio astronomy software packages, such as CASA v5.6[4] (McMullin et al. 2007; CASA Team 2022) and WSCLEAN v3[5] (Offringa et al. 2014). This pipeline handles first-generation calibration (1GC: cross-calibration and initial imaging), flagging, second-generation calibration (2GC: self-calibration and imaging), and third-generation calibration (3GC: direction-dependent calibration), following a structured approach that includes several key steps outlined below.

The first step involves initial calibration and flagging. The raw MeasurementSet (MS) is duplicated and averaged over 1024 channels to optimize continuum data processing and reduce computation time. Primary calibration begins by rephasing the primary calibrator using the CASA task `fixvis`, followed by radio frequency interference (RFI) flagging, where known RFI channels and contaminated bands (up to ∼40 per cent of the original bandwidth) are flagged using the CASA `flagdata` task and auto flaggers. Auto flagging tools, like `tfcrop` and `rflag` in CASA, along with the TRICOLOUR v0.1.8[6] package (Hugo et al. 2022), are employed to further clean the data of any residual RFI. The Stevens–Reynolds 2016 flux density scale (Partridge et al. 2016) is applied to the primary calibrator. Secondary calibration follows, constructing an intrinsic model for the secondary calibrator based on the primary calibrator data. Delay, bandpass, and gain calibrations are iteratively derived from both calibrators, and these solutions are applied to all calibrators and target data. These solutions are applied to the target data, ensuring calibration integrity through multiple rounds of residual flagging.

Following cross-calibration, the target data are imaged using WSCLEAN. A BRIGGS weighting (Briggs 1995) of −0.3 is used to balance noise sensitivity and angular resolution. WSCLEAN uses multiscale and wide-band deconvolution algorithms to improve the imaging of diffuse emission, deconvolving eight subband images with central frequencies of 909, 1016, 1123, 1230, 1337, 1444, 1551, and 1658 MHz, and generating a multifrequency synthesis map. Self-calibration is performed using the CUBICAL software (Kenyon et al. 2018), which refines calibration solutions through iterative reimaging and masking, significantly improving the images' dynamic range.

[3] https://github.com/IanHeywood/oxkat
[4] https://casa.nrao.edu
[5] https://sourceforge.net/p/wsclean/wiki/Home/
[6] https://github.com/ratt-ru/tricolour

Downloaded from https://academic.oup.com/mnras/article/542/2/1544/8230804 by Witwatersrand University user on 14 October 2025

Table 1. Properties of the first six clusters in the sample.

Cluster name (ACT-CL)	RA (J2000) ($^{h}:^{m}:^{s}$)	Dec. (J2000) ($^{\circ}:':''$)	Redshift z	Redshift type	$M_{500cCal,SZ}$ (10^{14} $M_{\odot}$)	$M_{500cUncorr,SZ}$ (10^{14} $M_{\odot}$)	SNR
J1137.8+0728	11:37:50.8	+07:28:36.0	1.01 ± 0.03	Phot[a]	$6.7^{+1.2}_{-1.1}$	$5.3^{+0.9}_{-0.7}$	16.9
J0546.6−5345	05:46:37.6	−53:45:33.2	1.07	Spec[b]	$6.0^{+1.1}_{-1.0}$	$4.7^{+0.8}_{-0.7}$	12.8
J2106.0−5844	21:06:04.3	−58:44:35.0	1.13	Spec[c]	$8.5^{+1.5}_{-1.4}$	$6.8^{+1.1}_{-0.9}$	18.7
J1142.7+1527	11:42:46.0	+15:27:22.0	1.19	Spec[d]	$6.3^{+1.1}_{-1.0}$	$5.0^{+0.8}_{-0.7}$	19.6
J0329.2−2330	03:29:17.7	−23:30:09.7	1.23	Spec[c]	$9.7^{+1.7}_{-1.6}$	$8.0^{+1.3}_{-1.1}$	22.1
J0003.9+1642	00:03:51.8	+16:42:06.5	1.31 ± 0.03	Phot[a]	$6.1^{+1.1}_{-1.0}$	$4.9^{+0.8}_{-0.7}$	14.7

Notes. The SZ values are obtained from the ACT DR5 catalogue (Hilton et al. 2021). Column (1): ACT DR5 cluster name; column (2): J2000 right ascension of the SZ centre; column (3): J2000 declination of the SZ centre; columns (4) and (5): redshift and redshift type of the cluster, respectively. The redshifts are sourced from: [a]zCluster (Hilton et al. 2021); [b]ACT (Macario et al. 2013; Sifón et al. 2016; Hilton et al. 2018); [c]SPT (Bocquet et al. 2019; Bleem et al. 2020); and [d]MaDCoWS (Gonzalez et al. 2015). Columns (6) and (7): ACT SZ mass calibrated using weak lensing and uncorrected ACT SZ mass, respectively. Note that the ACT SZ uncorrected mass is not corrected for Eddington bias and is used for comparison with *Planck* PSZ2 masses. Column (8): signal-to-noise ratio from ACT.

Table 2. Summary of MeerKAT *L*-band observations for the cluster sample, including observational parameters and both full-resolution (FR) and low-resolution (LR) imaging properties.

Cluster name (ACT-CL)	Observing date (yyyy-mm-dd)	Bandpass calibrator	Phase calibrator	Flagged (per cent)	$\theta_{synth,FR}$ (arcsec × arcsec, °)	$\sigma_{rms,FR}$ (μJy beam^{-1})	$\theta_{synth,LR}$ (arcsec × arcsec, °)	$\sigma_{rms,LR}$ (μJy beam^{-1})
J1137.8+0728[a]	2023-02-01	J0408−6545	J1150−0023	43.3	8.6 × 5.8, 174.1	4.8	15.5 × 15.5, 0.0	7.5
J0546.6−5345	2023-02-04	J0408−6545	J0538−4405	47.9	5.6 × 5.6, 0.0	6.1	15.2 × 15.2, 0.0	9.4
J2106.0−5844[a]	2022-12-19	J1939−6342	J1939−6342	52.3	9.0 × 5.3, 56.4	4.5	14.9 × 14.3, 130.3	6.5
J1142.7+1527	2023-02-04	J0408−6545	J1120+1420	43.2	7.9 × 7.9, 0.0	5.4	15.6 × 15.6, 0.0	7.2
J0329.2−2330[a]	2023-01-27	J0408−6545	J0409−1757	48.1	6.5 × 6.5, 0.0	5.0	15.2 × 15.2, 0.0	6.1
J0003.9+1642[a]	2023-01-29	J1939−6342	J2253+1608	44.7	10.2 × 5.5, 167.5	7.4	16.2 × 14.9, 175.1	9.2

Notes. Column (1): ACT DR5 cluster name; column (2): observation date; columns (3) and (4): bandpass and phase calibrators; column (5): the percentage of MeerKAT data that is flagged during reduction, which includes frequency ranges that are known to be affected by satellite interference; and columns (6)–(9): synthesized beam parameters (major and minor axes, and position angle) and central rms noise levels for both FR and LR images. [a]Direction-dependent corrections were required for the cluster field. The image shows significant variability in noise, attributed to residual contamination from the artefacts of the bright source.

For data sets where 2GC falls short in correcting direction-independent effects, resulting in images with significant residual artefacts, we employ direction-dependent calibration. The 3GC calibration step addresses direction-dependent effects (DDEs) in the radio interferometer measurement equation (RIME; Noordam & Smirnov 2010; Smirnov 2011a, b, c, d; Smirnov & Tasse 2015). For MeerKAT, major DDEs include primary beam rotation and pointing errors, which manifest as radial artefacts around bright sources. For wide-field imaging, phase and amplitude gains may vary significantly across the field of view, necessitating direction-dependent calibration. The OXKAT pipeline employs a facet-based approach using the KILLMS[7] (KMS; Tasse 2014a, b) and DDFACET[8] (DDF; Tasse et al. 2018) software to account for DDEs. The KMS tool performs 3GC by exploiting Wirtinger complex differentiation to directly estimate the physical DD RIME terms per facet, while DDF is a facet-based imager that can take into account KMS solutions to perform wide-band, wide-field differential spectral deconvolution.

2.4 Compact source subtraction

We performed the subtraction of compact sources to ensure that the flux density measurements of the diffuse emission remained uncontaminated by any compact source emissions. This process was carried out in the uv-plane, targeting all sources within the cluster radius (R_{500c}), centred at the cluster's SZ centre, using CRYSTALBALL v0.4.1[9] and MSUTILLS v1.2.0.[10] CRYSTALBALL uses a source list generated by WSCLEAN to create a model column in the MS file, containing only the tagged compact sources. The source list was generated from an image produced by WSCLEAN using a taper-inner-tukey of 10 kλ and Briggs weighting of 0 (see the left panel of Figs B1–B6), which effectively suppresses diffuse emission and isolates compact sources. MSUTILLS then subtracts this model column from the calibrated data column to create a new column of compact-source-subtracted visibilities. These visibilities are then used to produce low-resolution (LR) maps, enhancing the diffuse emission and ensuring no blending occurs between compact and extended emission.

2.5 Low-resolution maps

To enhance the detection of large-scale diffuse emission, we created LR images by applying an outer taper of ≤12 kλ, which corresponds to an angular resolution of ∼17.2 arcsec, or a physical scale of ∼139.5 kpc at the cluster redshift of $z = 1.01$, and using Briggs

[7]https://github.com/saopicc/killMS
[8]https://github.com/saopicc/DDFacet
[9]https://github.com/caracal-pipeline/crystalball
[10]https://github.com/SpheMakh/msutils

Downloaded from https://academic.oup.com/mnras/article/542/2/1544/8230804 by Witwatersrand University user on 14 October 2025

weighting with a robust parameter of 0 (see the right panel of Figs B1–B6). This approach gives more weight to shorter baselines, which are more sensitive to extended emission. The integrated flux densities were obtained from these LR images using polygon regions around each source, tracing the $3\sigma_{\rm rms}$ radio contours to comprehensively encompass the extent of the diffuse radio emission. The uncertainties of the flux densities of the diffuse radio sources are estimated using the expression

$$\Delta S_\nu = \sqrt{(\delta S_\nu \times S_\nu)^2 + N_{\rm beams}\sigma_{\rm rms}^2 + \sigma_{\rm sub}^2}, \quad (1)$$

where δS_ν represents the uncertainty in the absolute flux calibration, assumed to be 5 per cent for L-band, $N_{\rm beams}$ denotes the number of beams within the region where the flux density was measured, and $\sigma_{\rm rms}$ denotes the local rms noise of the image. The uncertainty attributable to compact-source subtraction, $\sigma_{\rm sub}$, is given by

$$\sigma_{\rm sub}^2 = \sum_i N_{{\rm beams},i}\sigma_{\rm rms}^2, \quad (2)$$

where the summation is taken over all the i sources that were subtracted within the polygon region surrounding the diffuse radio source, with $N_{{\rm beams},i}$ representing the number of beams covering the ith compact source.

The k-corrected radio power was calculated using the expression

$$P_{1.4\,\rm GHz} = 4\pi D_{\rm L}^2 \frac{S_{1.4\,\rm GHz}}{(1+z)^{\alpha+1}}, \quad (3)$$

where $S_{1.4\,\rm GHz}$ is the observed flux density scaled to 1.4 GHz, $D_{\rm L}$ is the luminosity distance, and α is the spectral index. While we attempted to produce in-band spectral index maps with L-band observations, the faintness of the emission made this challenging, and reliable maps could not be generated. Instead, we assume a Gaussian distribution for the spectral index α with a mean of -1.3 and a standard deviation of 0.4 for calculating the radio luminosity (Knowles et al. 2021). This assumption is based on the typical range of spectral indices observed in radio haloes, which often cluster around -1.3 but can vary. By using a Gaussian distribution, we account for the uncertainty in spectral indices and the possibility that they may be steeper than those found in local systems, which is consistent with observations of high-redshift clusters where the environment may influence the spectral properties.

3 RESULTS

In this section, we present the findings from the analysis of six galaxy clusters, focusing on their diffuse emission. Four of the clusters contain prominent diffuse emission that is visible in the full-resolution (FR) images (see Fig. 2). In the remaining two clusters, the diffuse emission is undetectable in FR images but becomes apparent only after compact source subtracted LR imaging (see Fig. 2). The detections meet the 3σ significance threshold, confirming the presence of diffuse emission. Below, we provide an overview of these results and highlight key features of the diffuse emission across the galaxy clusters. The measured properties are provided in Table 3.

3.1 Prominent diffuse emission

3.1.1 ACT-CL J2106.0−5844

ACT-CL J2106.0−5844 (hereafter ACT-CL J2106),[11] also known as SPT-CL J2106−5844, is among the most massive galaxy clusters identified at a high redshift of $z = 1.13$, with a mass of $M_{\rm 500cCal} = 8.5^{+1.5}_{-1.4} \times 10^{14}\,{\rm M}_\odot$. Initial observations using the South Pole Telescope (SPT; Carlstrom et al. 2011) revealed the cluster through its strong SZ effect signal, highlighting its significance as a unique object for studying galaxy formation and evolution, as well as for testing cosmological models (Foley et al. 2011). Further studies using the Atacama Large Millimeter/submillimeter Array and the Atacama Compact Array provided evidence of a bimodal structure in the pressure distribution of the ICM, strongly suggesting the cluster is undergoing a major merger (Di Mascolo et al. 2021).

Di Mascolo et al. (2021) identified diffuse radio emission associated with the cluster at 943 MHz as part of the Evolutionary Map of the Universe Pilot Survey (Norris et al. 2011). Di Mascolo et al. (2021) found a spatial correlation between optical star-forming filaments seen in *Hubble Space Telescope* (*HST*) images and small-scale jet-like radio structure, suggesting a potential connection between the radio jet and the ongoing star formation activity. Additionally, weak lensing studies using *HST* data have provided precise measurements of the cluster's mass distribution, which is highly asymmetric, consisting of a primary clump and a smaller subclump located approximately 640 kpc to the west (Kim et al. 2019; Di Mascolo et al. 2021).

In our analysis using the MeerKAT data, an LR image revealed a radio halo spanning approximately 0.98 × 0.93 Mpc in linear scale (see the top left panel of Fig. 2). The diffuse emission, measured within 3σ contours, has an integrated flux density of $S_{1.28\,\rm GHz} = 3.23 \pm 0.19$ mJy, corresponding to a k-corrected radio power at 1.4 GHz of $P_{1.4\,\rm GHz} = (3.78 \pm 1.34) \times 10^{24}\,{\rm W\,Hz^{-1}}$.

3.1.2 ACT-CL J1142.7+1527

ACT-CL J1142.7+1527 (hereafter ACT-CL J1142, alternative name: MOO J1142+1527) is a massive galaxy cluster located at $z = 1.19$, with a mass of $M_{\rm 500cCal} = 6.3^{+1.1}_{-1.0} \times 10^{14}\,{\rm M}_\odot$ as reported in the ACT DR5 catalogue. Initially identified in the Massive and Distant Clusters of *WISE* Survey (MaDCoWS; Gonzalez et al. 2015, 2019), its mass was later confirmed through SZ effect observations with the NIKA2 (New IRAM KID Arrays 2), which exhibited a decrement at a significance level of 13.2σ (Ruppin et al. 2020). The NIKA2 and MUSTANG-2 SZ observations reveal the cluster to be an exceptionally massive, hot, and unrelaxed merging system, with MUSTANG-2 confirming this MaDCoWS cluster at a significance level of 20.9σ (Dicker et al. 2020; Ruppin et al. 2020).

We observed diffuse radio emission at the centre of J1142 (see top right panel of Fig. 2). The integrated flux density is $S_{1.28\,\rm GHz} = 1.47 \pm 0.11$ mJy from the LR image, corresponding to a largest linear size (LLS) of 0.97 × 0.79 Mpc, with the k-corrected radio power scaled to 1.4 GHz of $P_{1.4\,\rm GHz} = (1.84 \pm 0.68) \times 10^{24}\,{\rm W\,Hz^{-1}}$. We classify the diffuse radio emission in J1142 as a radio halo since the emission is centrally located within the cluster, and displays a regular morphology that traces the X-ray-emitting ICM. The brightest radio source (∼200 kpc away from the SZ peak) flux density, which is $S_{1.28\,\rm GHz} = 37.27 \pm 1.85$ mJy, is consistent with the one found in Faint Images of the Radio Sky at Twenty-centimeters (37 mJy; Helfand, White & Becker 2015). Ruppin et al. (2020) suggested that J1142 might be undergoing a merger. Based on a multiwavelength analysis including *Chandra* X-ray and *NIKA2* SZ data, they further show that the central region of the cluster is hosting relatively cool gas, reminiscent of what could be the remnant cool core from one of the interacting systems.

[11] J2106 will be investigated in more detail in Perrott et al. (in preparation).

Downloaded from https://academic.oup.com/mnras/article/542/2/1544/8230804 by Witwatersrand University user on 14 October 2025

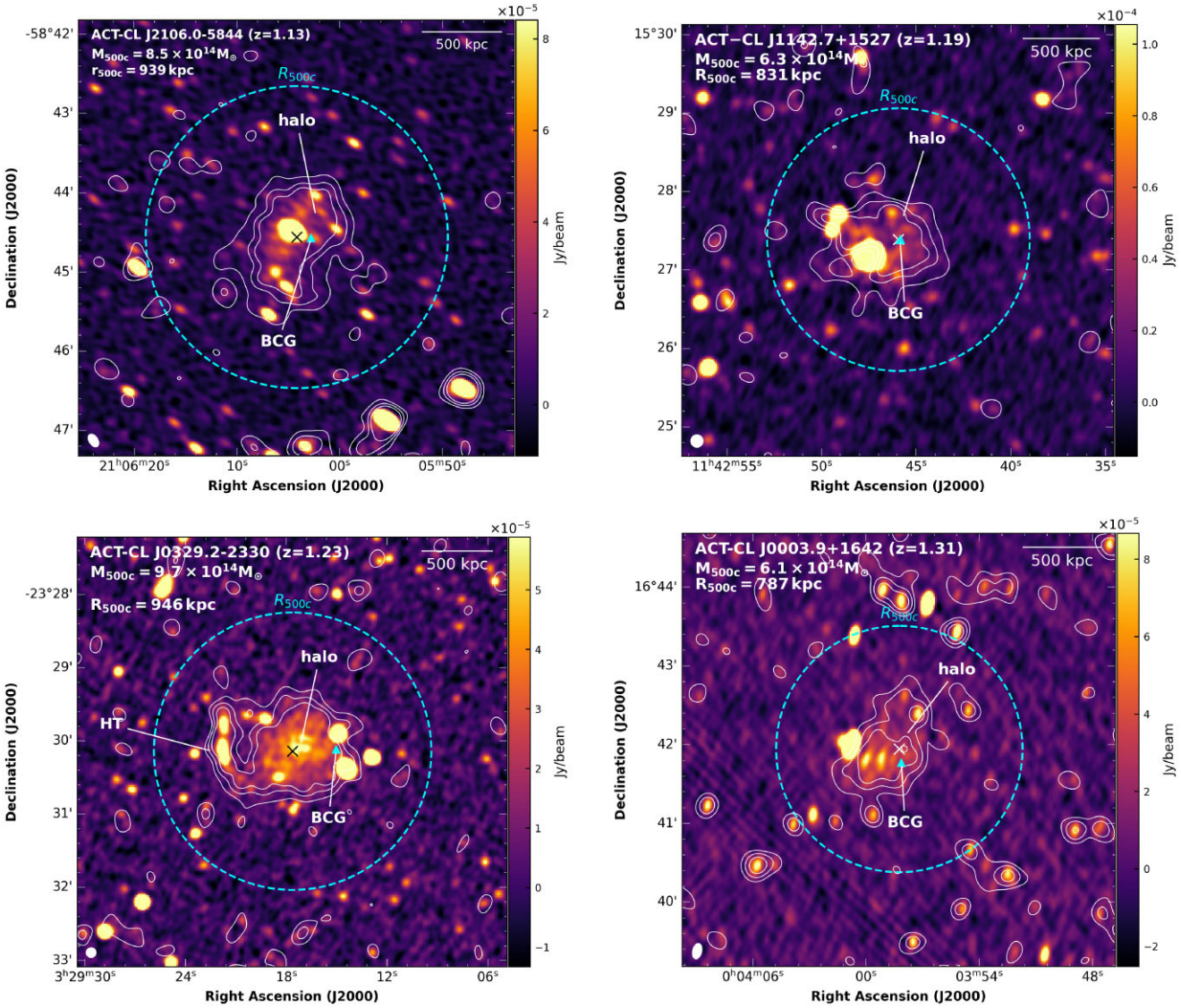

Figure 2. FR MeerKAT *L*-band images of clusters hosting radio haloes. The superimposed contours are from the LR source-subtracted images, with contour levels set at $\sigma_{\rm LR} \times [3, 6, 10]$. The projected physical scale at each cluster's redshift is indicated in the top right of each panel. The synthesized beam, shown as a filled white ellipse or circle, is displayed in the lower left corner of each panel, and the location of the ACT SZ peak is marked by the cross (black/white). The cyan triangle indicates the position of the BCG, adopted from the ACT DR5 catalogue (Hilton et al. 2021). Top left: ACT-CL J2106.0−5844 cluster, the FR image has a local rms of $1\sigma = 4.5\,\mu$Jy beam^{-1}, while the LR image used for the contours has a local rms of $1\sigma = 6.5\,\mu$Jy beam^{-1}. Top right: ACT-CL J1142.7+1527 cluster, the FR image has a local rms of $1\sigma = 5.4\,\mu$Jy beam^{-1}, while the LR image used for the contours has a local rms of $1\sigma = 7.2\,\mu$Jy beam^{-1}. Bottom left: ACT-CL J0329.2−2330 cluster, the FR image has a local rms of $1\sigma = 5.0\,\mu$Jy beam^{-1}, while the LR image used for the contours has a local rms of $1\sigma = 6.1\,\mu$Jy beam^{-1}. Bottom right: ACT-CL J0003.9+1642 cluster, the FR image has a local rms of $1\sigma = 7.4\,\mu$Jy beam^{-1}, while the LR image used for the contours has a local rms of $1\sigma = 9.2\,\mu$Jy beam^{-1}.

3.1.3 ACT-CL J0329.2−2330

ACT-CL J0329.2−2330, hereafter ACT-CL J0329, with a mass of $M_{\rm 500cCal} = 9.7^{+1.7}_{-1.6} \times 10^{14}$ M$_\odot$ and $z = 1.23$, is among the highest redshift galaxy clusters confirmed to host a radio halo (Sikhosana et al. 2025). J0329 was detected by both the ACT and SPT surveys, both of which use the SZ effect to identify distant, massive clusters (Bleem et al. 2020; Hilton et al. 2021).

Our analysis reveals a prominent radio halo located in the central region of the cluster. To the east, we observe a nearby elongated source that connects to the halo emission (see the left bottom panel of Fig. 2). This source exhibits a morphology consistent with a head–tail (HT) radio galaxy, and its flux density is 0.65 ± 0.01 mJy. The measured flux density of the halo is $S_{1.28\,\rm GHz} = 3.45 \pm 0.21$ mJy, excluding the tailed emission from the elongated source. The angular size of the halo is 2.17 arcmin × 1.73 arcmin, corresponding to a linear size of 1.08 × 0.86 Mpc. The *k*-corrected radio power at 1.4 GHz is $P_{1.4\,\rm GHz} = (4.51 \pm 1.68) \times 10^{24}$ W Hz^{-1}.

The findings are consistent with those of Sikhosana et al. (2025), who also detected a radio halo in ACT-CL J0329 with comparable flux density and angular/linear size characteristics. While the same MeerKAT *L*-band data were used in both studies, this work represents an independent analysis conducted using the OXKAT pipeline, distinct

Downloaded from https://academic.oup.com/mnras/article/542/2/1544/8230804 by Witwatersrand University user on 14 October 2025

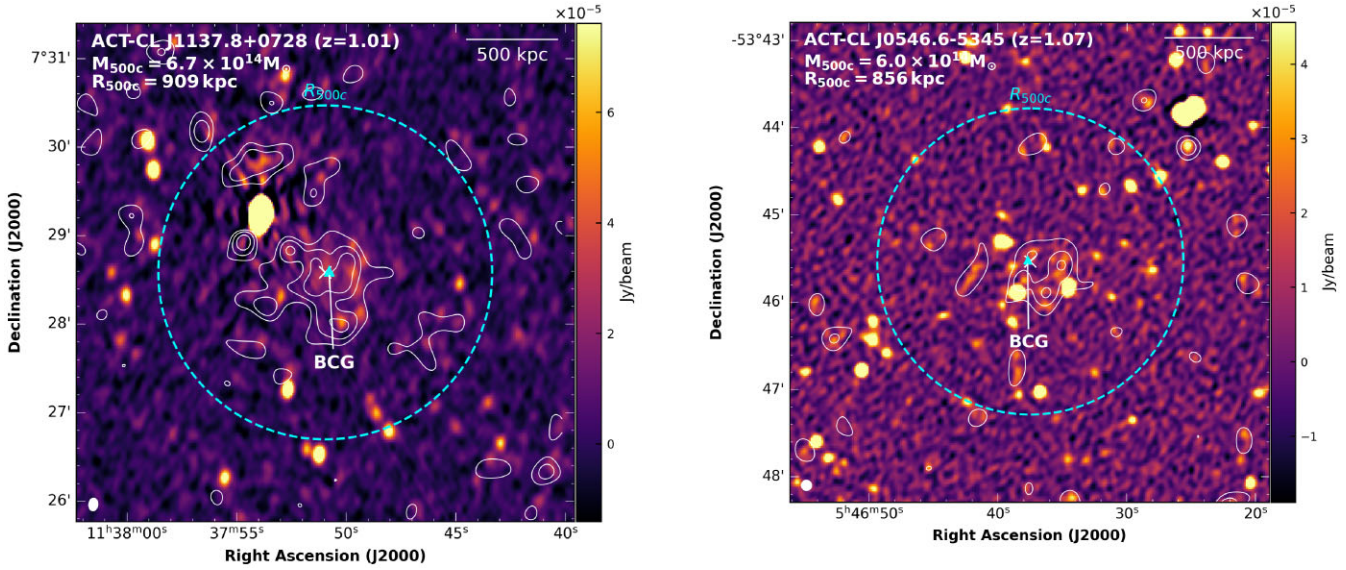

Figure 2. *Continued*. Left: ACT-CL J1137.8+0728 cluster, the FR image has a local rms of $1\sigma = 5.4\,\mu\text{Jy beam}^{-1}$, while the LR image used for the contours has a local rms of $1\sigma = 7.5\,\mu\text{Jy beam}^{-1}$. Right: ACT-CL J0546.6−5345 cluster, the FR image has a local rms of $1\sigma = 6.1\,\mu\text{Jy beam}^{-1}$, while the LR image used for the contours has a local rms of $1\sigma = 9.4\,\mu\text{Jy beam}^{-1}$.

Table 3. Measured properties of all detected diffuse emissions within the sample.

Cluster name (ACT-CL)	R_{500c} (kpc)	LAS (arcmin)	LLS (Mpc)	Classification	S_ν (mJy)	$P_{1.4\,\text{GHz}}$ ($\times 10^{24}$ W Hz^{-1})
J1137.8 + 0728	908.49	1.79 × 1.38	0.86 × 0.66	RH	0.87 ± 0.08	0.87 ± 0.29
J0546.6−5345	854.31	0.97 × 0.90	0.47 × 0.44	Uncertain	0.42 ± 0.04	0.46 ± 0.16
J2106.0−5844	939.07	1.99 × 1.88	0.98 × 0.93	RH	3.23 ± 0.19	3.78 ± 1.34
J1142.7+1527	829.06	1.96 × 1.59	0.97 × 0.79	RH	1.47 ± 0.11	1.84 ± 0.68
J0329.2−2330	951.05	2.17 × 1.73	1.08 × 0.86	RH	3.45 ± 0.21	4.51 ± 1.68
J0003.9+1642	786.96	1.96 × 1.51	0.99 × 0.76	RH	1.43 ± 0.12	2.03 ± 0.80

Notes. Column (1): ACT DR5 cluster name; column (2): R_{500c} of the mean mass overdensity of the cluster 500 times the cosmic critical density at the cluster redshift; column (3): largest angular size (LAS) of diffuse emission in arcmin; column (4): largest physical extent of diffuse emission at cluster redshift in Mpc; column (5): classification type: halo (RH); column (6): total flux density in mJy; and column (7): k-corrected radio power at 1.4 GHz, assuming $\alpha = -1.3 \pm 0.4$.

from the CARACAL[12] pipeline (Józsa et al. 2020) employed by Sikhosana et al. (2025). In addition, the elongated source to the east of the cluster's centre is identified as an HT radio galaxy. This HT galaxy provides valuable insights into the cluster's dynamical state and the possible merger history. The presence of such sources is often associated with dense ICM conditions and shocks generated by ongoing dynamical activity, further supporting the idea that the cluster has experienced significant merger-driven interactions (Sikhosana et al. 2025).

3.1.4 ACT-CL J0003.9+1642

Located at a redshift $z = 1.31$, ACT-CL J0003.9+1642 (hereafter ACT-CL J0003) is a galaxy cluster with a mass of $M_{500cCal} = 6.1^{+1.1}_{-1.0} \times 10^{14}\,M_\odot$, initially identified through the ACT's SZ effect measurements (Hilton et al. 2021). Our analysis of MeerKAT data reveals diffuse radio emission in the form of a radio halo concentrated near the cluster's centre (see bottom right panel of Fig. 2), spanning an angular size of 1.96 arcmin × 1.51 arcmin, which corresponds to a linear size of 0.99 × 0.76 Mpc. The integrated flux density of the diffuse emission is measured to be $S_{1.28\,\text{GHz}} = 1.43 \pm 0.12$ mJy, translating to a k-corrected radio power of $P_{1.4\,\text{GHz}} = (2.03 \pm 0.80) \times 10^{24}\,\text{W Hz}^{-1}$.

The brightest radio source in the image, located ∼38 arcsec east of the halo's central peak (projected distance ∼317 kpc), shows a flux density of 2.83 ± 0.14 mJy. This offset compact source is distinct from the BCG visible in optical counterparts (Fig. A2). It is spatially coincident with a point-like, pink-coloured optical source, suggesting it is likely a foreground star unrelated to the diffuse emission. The BCG itself is located <20 arcsec from the SZ peak position in the south. The presence of the central radio halo nevertheless indicates merger-driven turbulence (Feretti et al. 2012; Weeren et al. 2019), potentially from a recent minor merger or line-of-sight accretion event that preserved the overall cluster symmetry.

3.2 Faint diffuse emission

3.2.1 ACT-CL J1137.8+0728

The galaxy cluster ACT-CL J1137.8+0728 (hereafter ACT-CL J1137), located at a redshift of $z = 1.01$, has a total estimated mass of $M_{500cCal} = 6.7^{+1.5}_{-1.4} \times 10^{14}\,M_\odot$. The initial FR MeerKAT image showed no evidence of diffuse emission, limited by the low

[12] https://github.com/caracal-pipeline/caracal

Downloaded from https://academic.oup.com/mnras/article/542/2/1544/8230804 by Witwatersrand University user on 14 October 2025

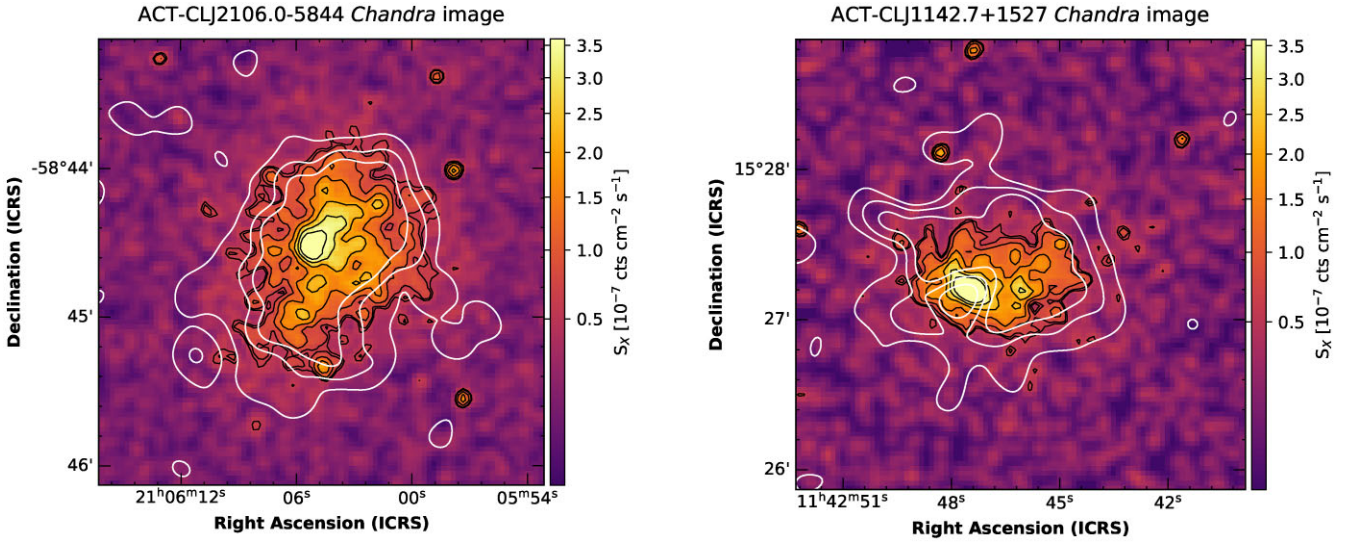

Figure 3. *Chandra* exposure-corrected images were created using the 0.7–7.0 keV energy band and observed using ACIS-I in VFAINT mode exposure-corrected images. For the purpose of display, the images were 4 × 4 pixels binned to 1.968 arcsec resolution and then smoothed with a Gaussian kernel of 1 pixel full width at half-maximum (FWHM). The black contours trace the X-ray surface brightness at levels of [0.6, 0.69, 0.98, 1.5, 2.1, 3.0, 4.0] × 10^{-7} counts cm^{-2} s^{-1}. The white superimposed contours from the MeerKAT LR image are shown at levels of $\sigma \times [3, 6, 10]$, where 1σ corresponds to 6.5 μJy $beam^{-1}$ of the J2106 cluster (left) and 7.2 μJy $beam^{-1}$ for J1142 cluster (right). The left panel shows the J2106 cluster *Chandra* image, generated from observation IDs 12180 and 12189 (PI: S. Murray and G. Garmire) with an exposure time of 24.72 and 48.13 ks, respectively. The right panel shows the J1142 cluster *Chandra* image, generated from observation ID 18277 (PI: S. Stanford) with an exposure time of 46.95 ks.

surface brightness of the ICM. However, after applying point-source subtraction and reimaging with lower resolution techniques, faint diffuse radio emission emerged, reaching a significance threshold of 3σ.

The measured flux density of diffuse emission is $S_{1.28\,\mathrm{GHz}} = 0.87 \pm 0.08$ mJy, and the k-corrected radio power of the halo is $P_{1.4\,\mathrm{GHz}} = (0.87 \pm 0.29) \times 10^{24}$ W Hz^{-1}. The diffuse emission extends across a region that is centred on the core of the cluster, as shown in Fig. 2. The cyan dashed circle represents $R_{500c} = 908$ kpc, and the detected emission lies within this region. The brightest radio source is located approximately 60 arcsec north-east of the SZ peak centre, with a flux density of $S_{1.28\,\mathrm{GHz}} = 39.23 \pm 1.96$ mJy. Despite the use of direction-dependent calibration, residual artefacts from this bright source are visible in the image and extend toward the central region of the cluster. While these artefacts are largely suppressed, they may contribute marginally to the measured flux of the diffuse emission.

3.2.2 ACT-CL J0546.6−5345

ACT-CL J0546.6−5345 (hereafter ACT-CL J0546, also known as SPT−CL J0546.6−5345) is a galaxy cluster located at $z = 1.07$, with an estimated mass of $M_{500cCal} = 6.0^{+1.1}_{-1.0} \times 10^{14}$ $M_\odot$. It was initially detected through its SZ effect signature in a survey conducted using the SPT. The initial detection was reported by Staniszewski et al. (2009), and subsequent confirmation and analysis were conducted by Brodwin et al. (2010).

Using MeerKAT observations, faint diffuse radio emission was identified within the cluster. Although the emission was not visible in the FR image, the subtraction of compact sources in the LR data revealed the diffuse component at the 3σ level (see Fig. 2). The measured flux density of the emission is $S_{1.28\,\mathrm{GHz}} = 0.42 \pm 0.04$ mJy, which yields a k-corrected radio power of $P_{1.4\,\mathrm{GHz}} = (0.46 \pm 0.16) \times 10^{24}$ W Hz^{-1}. ACT-CL J0546 exhibits faint, patchy radio emission tracing individual galaxies rather than the ICM. While statistically significant at 3σ, the emission lacks the spatial extent (≥0.5 Mpc) and central concentration required for a radio halo classification (Cassano et al. 2010). This emission likely originates from AGN activity or fossil plasma from past minor mergers, consistent with its near-relaxed X-ray morphology (see Fig. 6). Given the absence of a clear, centrally located, and Mpc-scale emission feature, we classify the radio emission in ACT-CL J0546 as uncertain.

3.3 Dynamical state of the galaxy clusters

Galaxy clusters are dynamically evolving systems, continuously accreting matter, and undergoing mergers throughout cosmic time. While they are often categorized as relaxed or disturbed for observational convenience, these labels represent endpoints on a spectrum of dynamical states rather than discrete classes. Relaxed clusters typically have a symmetrical distribution of galaxies and intracluster gas around their BCG, indicating they have reached a state of approximate virial equilibrium. In contrast, dynamically disturbed clusters deviate significantly from virial equilibrium, often displaying substructure, multiple bright galaxies, and irregular X-ray morphologies. The presence and morphology of diffuse radio emission are closely linked to the dynamic state, as mergers and disturbances can inject turbulence into the ICM, leading to the (re)acceleration of CRe (Cassano et al. 2010).

The *Chandra* X-ray data were obtained from the *Chandra* Data Archive[13] (ObsIDs listed in Figs 3–5). Observations were conducted with the Advanced CCD Imaging Spectrometer – Imaging array (ACIS-I) in very faint (VFAINT) mode, spanning 0.7–7.0 keV. Data reduction followed standard procedures using *Chandra* Interactive Analysis of Observations (CIAO v4.15; Fruscione et al. 2006)[14] and

[13] http://cda.harvard.edu/chaser/
[14] https://cxc.cfa.harvard.edu/ciao/download/

Downloaded from https://academic.oup.com/mnras/article/542/2/1544/8230804 by Witwatersrand University user on 14 October 2025

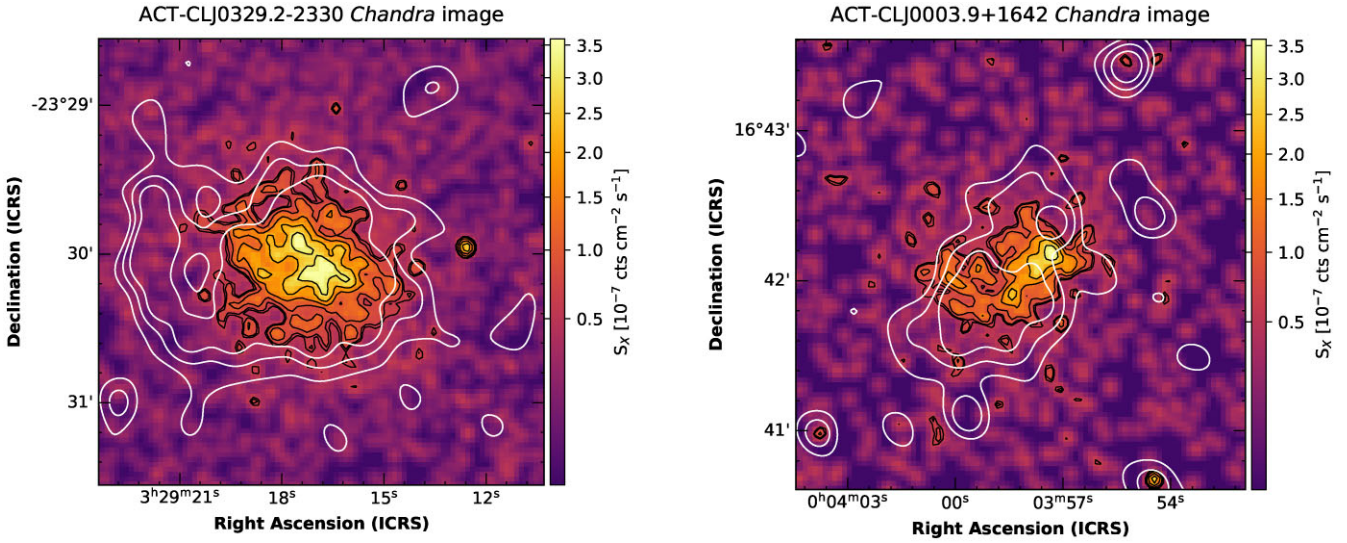

Figure 4. *Chandra* exposure-corrected images were created using the 0.7–7.0 keV energy band and observed using ACIS-I in VFAINT mode exposure-corrected images. For the purpose of display, the images were 4 × 4 pixels binned to 1.968 arcsec resolution and then smoothed with a Gaussian kernel of 1 pixel FWHM. The black contours trace the X-ray surface brightness at levels of [0.6, 0.69, 0.98, 1.5, 2.1, 3.0, 4.0] × 10^{-7} counts cm^{-2} s^{-1}. The white superimposed contours from the MeerKAT LR image are shown at levels of σ × [3, 6, 10], where 1σ corresponds to 6.1 μJy beam^{-1} of the J0329 cluster (left) and 9.2 μJy beam^{-1} for J0003 cluster (right). The left panel shows the J0329 cluster *Chandra* image, generated from observation IDs 18282 and 18882 (PI: L. Bleem) with an exposure time of 26.14 and 21.37 ks, respectively. The right panel shows the J0003 cluster *Chandra* image, generated from observation ID 26935 (PI: A. Flores) with an exposure time of 19.80 ks.

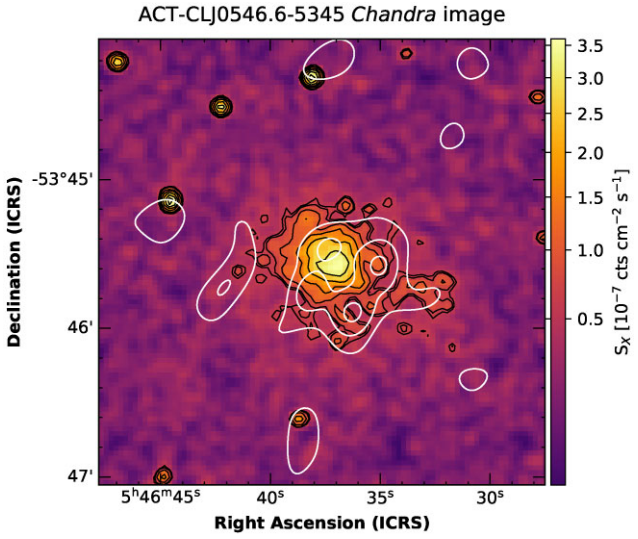

Figure 5. *Chandra* exposure-corrected images were created using the 0.7–7.0 keV energy band and observed using ACIS-I in VFAINT mode exposure-corrected images. For the purpose of display, the image was 4 × 4 pixels binned to 1.968 arcsec resolution and then smoothed with a Gaussian kernel of 1 pixel FWHM. The J0546 cluster *Chandra* image, generated from observation IDs 9332, 10851, 10864, 9336, and 11739 (PI: G. Garmire and J. Mohr) with an exposure time of 14.88, 8.52, 5.76, 28.17, and 12.78 ks, respectively. The black contours trace the X-ray surface brightness at levels of [0.6, 0.69, 0.98, 1.5, 2.1, 3.0, 4.0] × 10^{-7} counts cm^{-2} s^{-1}, and the white superimposed contours from the MeerKAT LR image have contour levels of σ × [3, 6, 10], with 1σ = 9.4 μJy beam^{-1}.

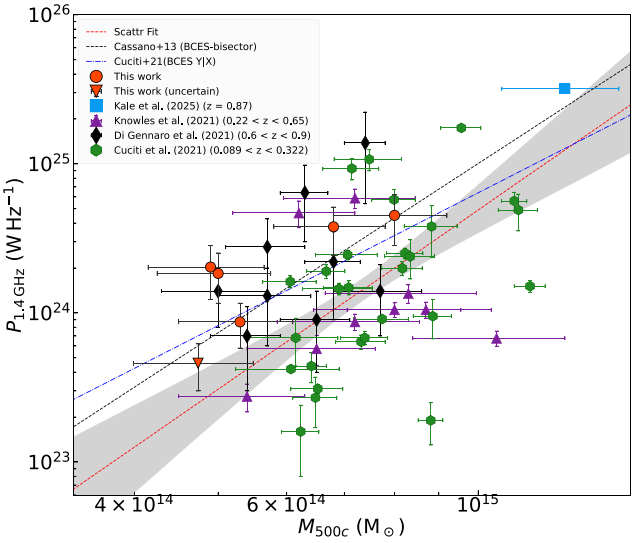

Figure 6. $P_{1.4\,GHz}$–M^{unc}_{500c} correlation plot for radio haloes listed in Table 2. To address discrepancies between the mass estimates from ACT and *Planck*, we use the uncorrected M_{500c} values from ACT DR5 (Hilton et al. 2021). The sample from Di Gennaro et al. (2021) includes radio haloes at $z > 0.6$, while the sample from Knowles et al. (2021) spans $0.22 < z < 0.65$. The green hexagonal points represent the sample from Cuciti et al. (2021) covering $0.089 < z < 0.322$. Additionally, the cluster El Gordo, located at $z = 0.87$, is incorporated into the analysis (Kale et al. 2025). The red dashed line and shaded regions represent the SCATTR best fit, with its 95 per cent confidence interval. We also show the $P_{1.4\,GHz}$–M_{500c} correlations from Cuciti et al. (2021, blue dot–dashed line) and Cassano et al. (2013, black dashed line), scaled to 1.4 GHz. Note that the ACT SZ uncorrected masses plotted here are not corrected for Eddington bias, enabling direct comparison with *Planck* PSZ2 masses.

Downloaded from https://academic.oup.com/mnras/article/542/2/1544/8230804 by Witwatersrand University user on 14 October 2025

calibration data base (CALDB v4.12.0; Graessle et al. 2007).[15] Of the six clusters in our sample, five have archival *Chandra* X-ray data, and ACT-CL J1137 lacks X-ray observations. To assess the dynamical state of each cluster, we adopt the morphological classification scheme defined by Yuan & Han (2020) and Yuan et al. (2022), which uses a combination of X-ray morphological indicators.

3.3.1 ACT-CL J2106.0−5844

The *Chandra* X-ray image of ACT-CL J2106 (Fig. 3, left panel) shows clear signs of a dynamically disturbed morphology, with asymmetric emission and a tail-like feature extending to the north-west, which are indicative of an ongoing merger. Although the BCG lies near the X-ray peak (offset by <5 kpc), this spatial alignment does not preclude merger activity. The combination of the disturbed X-ray structure and the presence of a central radio halo suggests active turbulence in the ICM, which is commonly associated with merging systems. The radio halo broadly traces the thermal X-ray emission and points to merger-driven processes that reaccelerate relativistic particles (Brunetti & Jones 2014; Weeren et al. 2019). Constraining the geometry of the merger more precisely would require additional probes, including galaxy velocity distributions, detailed X-ray temperature maps, and the spatial alignment of substructures.

3.3.2 ACT-CL J1142.7+1527

The *Chandra* X-ray image reveals a moderately elongated morphology with asymmetric substructure in the core region (see the right panel of Fig. 3). The BCG is spatially coincident with the SZ peak but offset by ∼200 kpc from both the X-ray emission peak and the large-scale ICM centroid. This triple offset, BCG/SZ peak, X-ray emission peak, and ICM centroid, indicates ongoing merger activity, as relaxed clusters typically exhibit alignment between these components. The MeerKAT radio halo shows (Fig. 2, right panel) a centroid offset of 10–20 arcsec (∼150–300 kpc) from the BCG, aligning more closely with the ICM centroid. This spatial relationship implies the halo traces turbulent motions in the bulk ICM rather than being directly tied to the BCG's position.

3.3.3 ACT-CL J0329.2−2330

The *Chandra* X-ray image reveals a moderately elongated morphology along the north-east–south-west direction with asymmetric substructure in the core region (see the left panel of Fig. 4). This morphology suggests a dynamically disturbed state. The X-ray image exhibits significant asymmetry and an irregular shape. Furthermore, the radio contours indicate that the radio halo emission is generally colocated with the X-ray emission, providing evidence for recent or ongoing merger activity that likely generates the observed turbulence and diffuse radio emission.

3.3.4 ACT-CL J0003.9+1642

The X-ray emission from ACT-CL J0003 (see the right panel of Fig. 4) displays a notably irregular and elongated morphology, with some possible substructure evident. The BCG is located within 20 arcsec of the SZ peak toward the south. Despite this proximity, the distorted X-ray morphology and the presence of a central radio halo suggest that the cluster is dynamically disturbed. These features indicate that merger-driven turbulence is likely impacting the distribution of the ICM, possibly as a result of ongoing or recent merger activity.

3.3.5 ACT-CL J0546.6−5345

ACT-CL J0546.6−5345 presents an intriguing case. The *Chandra* X-ray image (see Fig. 5) shows a nearly relaxed morphology with a central peak of X-ray emission, suggesting the ICM is quite symmetrical and possibly nearly virialized. However, we note a clear spatial offset between the peak of the X-ray emission and the centroid of the radio emission. Such an offset is atypical for relaxed clusters and may signal ongoing dynamical activity or projection effects. This cluster was classified as dynamically disturbed by Yuan & Han (2020) and Yuan et al. (2022), based on the morphology index. Morphology index, δ, is based on X-ray surface brightness fluctuations where $\delta \geq 0$ indicates disturbed systems and $\delta < 0$ indicates relaxed clusters (Yuan & Han 2020). For ACT-CL J0546.6−5345, the morphology index δ is above zero, implying disturbance. Additionally, velocity dispersion analysis of cluster galaxies from Sifón et al. (2016) reveals significant dynamical disturbance via the Dressler–Shectman test (Dressler & Shectman 1988), inconsistent with a relaxed system. This discrepancy between X-ray and optical data could indicate a line-of-sight merger, where the collision axis aligns with our viewing direction (Mann & Ebeling 2012). In such geometry, the X-ray morphology remains symmetric due to projection effects, while galaxy kinematics retain merger-induced velocity anisotropies.

The radio emission from MeerKAT data appears to be tracing individual radio galaxies within the cluster rather than a diffuse radio halo. The lack of a clear radio halo is consistent with one possible interpretation where an edge-on (line-of-sight) merger geometry reduces the observable turbulent reacceleration, limiting radio halo formation or its detectability (Mann & Ebeling 2012). None the less, it is also possible that this cluster simply does not host a radio halo, or that any halo is too faint to be detected at the current MeerKAT *L*-band sensitivity (see Cassano et al. 2013; Cuciti et al. 2021, for occurrence rates and detection thresholds at higher redshifts). The system likely represents an early-stage merger where bulk motions dominate over shock-driven turbulence, rather than a post-merger relaxing system.

4 DISCUSSION

Our analysis of six most massive high-redshift clusters selected based on their SZ mass reveals a 83 per cent detection rate of diffuse radio emission, providing further insights into the dynamical states and ICM processes of these clusters. By plotting the scaling relation $P_{1.4\,\mathrm{GHz}}$ versus M^{unc}_{500c} (see Fig. 6), we find that the measured radio halo powers align broadly with the established trends observed in clusters with lower redshifts. We use uncorrected SZ masses (M^{unc}_{500c}) for consistency with the $P_{1.4\,\mathrm{GHz}}$–M_{500} correlation literature (Cassano et al. 2013; Cuciti et al. 2023). These masses derive directly from the universal pressure profile scaling relation (Arnaud et al. 2010) without weak lensing calibration adjustments, avoiding systematic uncertainties from mass bias corrections (Hilton et al. 2021).

[15] https://cxc.cfa.harvard.edu/caldb/

Downloaded from https://academic.oup.com/mnras/article/542/2/1544/8230804 by Witwatersrand University user on 14 October 2025

4.1 Characteristics of prominent radio haloes

The prominent radio haloes detected in this study exhibit key characteristics that align with expectations for diffuse emission in merging galaxy clusters. These haloes are extended, low surface brightness features that trace the thermal ICM. Their spatial extent ranges from approximately 0.97 to 1.08 Mpc, consistent with typical sizes observed in lower redshift clusters. The measured flux densities of the haloes span 1.43–3.45 mJy at 1.28 GHz, corresponding to k-corrected radio powers scaled to 1.4 GHz in the range 1.84×10^{24} to 4.51×10^{24} W Hz^{-1}.

The radio haloes are spatially coincident with X-ray emission from the ICM, as confirmed by *Chandra* observations. This colocation aligns with the disturbed X-ray morphologies, characterized by asymmetries and substructures observed in these clusters, which indicate dynamically active systems. Together, these features support the model where merger-driven turbulence reaccelerates CRe and amplifies magnetic fields, generating the observed synchrotron emission (Cassano et al. 2010; Brunetti & Jones 2014).

4.2 Properties of faint radio haloes

The clusters ACT-CL J1137 and ACT-CL J0546 highlight the critical role of MeerKAT's sensitivity combined with advanced imaging techniques (e.g. compact source subtraction and LR mapping) in detecting faint diffuse radio emission at high redshifts. These systems exhibit lower radio powers, with $P_{1.4\,\mathrm{GHz}} = (0.46\text{–}0.87) \times 10^{24}$ W Hz^{-1}, placing them at the faint end of the $P_{1.4\,\mathrm{GHz}}$–M^{unc}_{500c} scaling relation. Notably, these clusters also represent the lowest mass systems in our sample, consistent with the expectation that turbulent reacceleration scales with cluster mass (Cassano et al. 2010, 2013). Higher mass mergers generate stronger turbulence within the ICM, amplifying magnetic fields and enhancing synchrotron radiation efficiency (Brunetti & Jones 2014). The faint emissions observed in these clusters reflect the reduced turbulence and weaker magnetic field amplification associated with their lower masses.

In ACT-CL J1137, faint diffuse emission emerges only after compact source subtraction, appearing centrally located and broadly aligned with the cluster's SZ peak. While its low power and limited extent place it at the faint end of the radio halo population, the marginal detection significance warrants cautious interpretation and further observational follow-up. ACT-CL J0546 presents a classification challenge. Although statistically significant diffuse emission is detected at the 3σ level after compact source subtraction, the morphology is patchy and appears to trace individual galaxies rather than a centrally concentrated ICM component. Archival *Chandra* X-ray data reveal a near-symmetric and relaxed ICM morphology, and no spatial correlation is observed between the radio emission and the X-ray structure (Fig. 5). These factors, combined with its optical morphology (right panel Fig. A3), suggest a near-relaxed dynamical state and limited turbulent activity.

Despite their faintness, these detections confirm that diffuse radio emission persists in the most massive, high-redshift clusters. The localization of emission within r_{500c} in these systems suggests a strong connection between the thermal and non-thermal components of the ICM. This connection is further supported by their alignment with the $P_{1.4\,\mathrm{GHz}}$–M^{unc}_{500c} scaling relation, even at the low-power end.

These faint radio haloes, detected only after careful compact source subtraction and LR imaging, underscore the observational challenges of studying diffuse emission at high redshift. Our results highlight the importance of deeper and more sensitive observations to probe the faint end of the radio halo population and to advance our understanding of turbulence and magnetic field evolution in distant clusters.

4.3 Scaling relation and implications

The $P_{1.4\,\mathrm{GHz}}$–M^{unc}_{500c} scaling relation is an important tool for probing the link between a galaxy cluster's mass and its non-thermal radio emission. Our observations, represented by red points in Fig. 6, extend the existing data on this relationship to higher redshifts ($z > 1$; see Table 1 for redshift values) and demonstrate that these high-redshift clusters scatter around the established trend measured at $z \sim 0.2$ (Cassano et al. 2013). Notably, while Fig. 6 does not explicitly show a strong redshift evolution, there appears to be a mild systematic offset. The data from Knowles et al. (2021) mostly lie below the dashed line, whereas our data and those from Di Gennaro et al. (2021) lie above it. This pattern could suggest a mild redshift dependence, possibly reflecting evolving turbulence and magnetic field strengths in the ICM. If turbulent reacceleration remains the dominant mechanism, this may imply stronger magnetic fields and turbulence levels at higher redshifts. Given that IC losses are higher at high redshift, maintaining radio halo luminosities comparable to low-z systems requires either enhanced turbulent energy injection or magnetic field strengths higher than in local clusters, as predicted by turbulent reacceleration models (Di Gennaro et al. 2021).

To quantify the relationship, we performed a linear regression in log–log space using the SCATTR[16] method, which accounts for intrinsic scatter and measurement uncertainties in both variables. The results of the fit are reported in Table C1, Our analysis combines our data with low-redshift samples from Di Gennaro et al. (2021) and Knowles et al. (2021). The results confirm that radio halo power increases steeply with cluster mass, consistent with previous findings. This steep scaling is often attributed to the increased turbulence present in massive, merging clusters, which efficiently accelerates relativistic particles and amplifies magnetic fields within the ICM, leading to enhanced synchrotron radiation.

Our findings are consistent with previous studies (Cassano et al. 2010, 2013; Cuciti et al. 2021, 2023) that link mergers to the $P_{1.4\,\mathrm{GHz}}$–M^{unc}_{500c} scaling relation. As shown in Fig. 6, the clusters in our sample populate the same region of this plane as lower redshift systems, consistent with turbulent reacceleration as the dominant mechanism. However, while our data support this model, they do not definitively rule out alternative scenarios such as hadronic processes. Hadronic models, which posit that secondary electrons from proton–proton collisions produce synchrotron emission, predict a steeper dependence of radio power on cluster mass (Brunetti & Blasi 2005; Brunetti & Jones 2014). Furthermore, given our small sample size (six clusters), it remains challenging to disentangle mass and redshift effects definitively. Future studies with larger samples will be essential to better constrain these dependencies and explore potential deviations at $z > 1$.

4.4 SZ mass boosts in merging clusters

The dynamical disturbance observed in 80 per cent of our sample (4/5 clusters with X-ray data) has critical implications for SZ mass estimates. Hydrodynamical simulations demonstrate that mergers transiently enhance the integrated SZ signal (by ∼10–30 per cent) due to shock-driven increases in thermal pressure, with these boosts persisting for $\sim 0.5 - 1$ Gyr post-collision (Randall et al. 2008; Wik

[16] https://github.com/lucadimascolo/scattr

Downloaded from https://academic.oup.com/mnras/article/542/2/1544/8230804 by Witwatersrand University user on 14 October 2025

et al. 2008). At high redshifts ($z > 1$), where mergers dominate hierarchical growth (Poole et al. 2007; Véliz Astudillo et al. 2025), such pressure enhancements may lead to inflated SZ-derived mass estimates compared to relaxed systems. Our sample, selected for high-SZ masses ($M_{500c} > 4.5 \times 10^{14}$ M$_\odot$), likely represents systems where merger-driven pressure boosts contribute to elevated M^{SZ}_{500c} values.

Critically, diffuse radio emission is detected in all six clusters, with four hosting prominent radio haloes and two showing faint detections (see Sections 3.1 and 3.2). The observed radio halo powers ($P_{1.4\,GHz} \sim 0.5$–4.5×10^{24} W Hz^{-1}) align with turbulent reacceleration models (Cassano et al. 2010), providing empirical evidence that the same mergers that may drive transient SZ signal boosts also inject sufficient turbulence to sustain radio haloes. However, the faint detections (ACT-CL J1137 and J0546) require further investigation. Notably, ACT-CL J0546 exhibits a relaxed X-ray morphology but shows faint, patchy radio emission that may originate from AGN activity or fossil plasma from a minor merger rather than merger-driven turbulence (e.g. Savini et al. 2019; Brienza et al. 2022). This suggests that while mergers dominate the sample, secondary processes may contribute to non-thermal emission in some high-z clusters. The synergy between SZ and radio observations reinforces simulations showing that merger boosts preferentially select massive, dynamically active clusters in high-z SZ catalogues (Wik et al. 2008; Krause et al. 2012).

5 SUMMARY AND CONCLUSIONS

In this study, we presented the results of a search for diffuse radio emission in six massive galaxy clusters at redshifts $z > 1$, selected from the MMDCS. These six clusters represent the most massive systems in the sample, as determined by their SZ mass, and the full MMDCS sample will be analysed in future work. Using advanced imaging techniques, including compact source subtraction and LR mapping, we detected diffuse radio emission in four clusters (ACT-CL J2106, J1142, J0329, and J0003) and identified faint emission in two additional systems (ACT-CL J1137 and J0546). The radio haloes exhibit a range of linear sizes from 0.47 to 1.08 Mpc and radio powers spanning $P_{1.4\,GHz} = (0.46 \pm 0.16) \times 10^{24}$ to $(4.51 \pm 1.68) \times 10^{24}$ W Hz^{-1}. These results extend the known population of radio haloes into the high-redshift regime, demonstrating that diffuse synchrotron emission persists in massive clusters even under the challenging conditions imposed by increased IC losses at $z > 1$.

The dynamical states of the clusters were investigated using *Chandra* X-ray imaging combined with MeerKAT radio observations. Four clusters (ACT-CL J2106, J1142, J0329, and J0003) display disturbed X-ray morphologies characterized by asymmetries, elongation, and substructure, which are features indicative of ongoing or recent merger activity. These systems host prominent radio haloes tracing turbulent regions within R_{500c}, reinforcing the connection between mergers and non-thermal processes in the ICM. In contrast, ACT-CL J0546 exhibits a relaxed morphology with no clear halo signature, while ACT-CL J1137 remains unknown due to the lack of X-ray data.

The scaling relation between radio halo power and cluster mass ($P_{1.4\,GHz}$–M^{unc}_{500c}) was analysed, revealing that our high-redshift sample aligns with trends observed at lower redshifts, supporting turbulent reacceleration as the dominant mechanism for radio halo formation. While no explicit redshift-dependent trend was observed, our data points are consistent with the low-redshift, high-mass region of the scaling relation. This suggests mergers in massive clusters inject sufficient turbulence to sustain luminous haloes despite enhanced energy losses due to the CMB. The faint radio emission in ACT-CL J0546 might reflect reduced turbulent activity in relaxed systems, consistent with models where merger-driven shocks dominate particle acceleration. However, the scarcity of confirmed relaxed clusters at $z > 1$ currently limits conclusions about this relationship. The consistency of the $P_{1.4\,GHz}$–M^{unc}_{500c} scaling relation across redshifts supports turbulent reacceleration as the dominant mechanism for radio halo formation in merging clusters. Mergers are essential for generating the turbulence required to power radio haloes, as evidenced by the disturbed dynamical states of the majority of our sample. While hydrodynamical simulations suggest merger-driven thermal pressure boosts can temporarily elevate SZ masses by ~10–30 per cent (Wik et al. 2008; Krause et al. 2012), this transient effect does not uniformly bias SZ-derived masses. Relaxed clusters, though less common in high-z SZ surveys, may exhibit brighter radio emission from AGN or cool-core-related processes, highlighting the complex interplay between dynamical state and non-thermal emission mechanisms.

In conclusion, our findings demonstrate MeerKAT's unique capability to detect faint diffuse emission in high-redshift clusters, providing critical insights into the interplay between cluster mass, dynamical state, and non-thermal processes in the early universe. However, spectral index measurements remain challenging due to current sensitivity limits. Diffuse radio emission is detected in all six clusters (four prominent haloes, two faint), underscoring the prevalence of merger-driven turbulence in massive $z > 1$ systems. Future observations at lower frequencies (e.g. MeerKAT's *UHF* band) will be essential for constraining magnetic field strengths and electron energy loss mechanisms through detailed spectral studies. Expanding the analysis to the full MMDCS sample of 30 clusters will clarify whether the high detection rate persists across a broader mass range or reflects a unique property of the most extreme $z > 1$ mergers. This will enable a comprehensive investigation into the evolution and growth of magnetic fields across cosmic time, shedding light on how these fields develop in massive galaxy clusters.

ACKNOWLEDGEMENTS

The MeerKAT telescope is operated by the South African Radio Astronomy Observatory (SARAO), which is a facility of the National Research Foundation, an agency of the Department of Science and Innovation, South Africa. The financial assistance of the SARAO towards this research is hereby acknowledged. MH, KM, and US acknowledge support from the National Research Foundation of South Africa.

DATA AVAILABILITY

The raw data underlying this article are available in SARAO archive under the proposal ID SCI-20220822-MH-01, at https://archive.sarao.ac.za.

REFERENCES

Arnaud M., Pratt G. W., Piffaretti R., Böhringer H., Croston J. H., Pointecouteau E., 2010, A&A, 517, A92
Bleem L. E. et al., 2020, ApJS, 247, 25
Bocquet S. et al., 2019, ApJ, 878, 55
Böhringer H. et al., 2000, ApJS, 129, 435
Botteon A., Gastaldello F., Brunetti G., Dallacasa D., 2016, MNRAS, 460, L84
Brienza M. et al., 2022, A&A, 661, A92

Downloaded from https://academic.oup.com/mnras/article/542/2/1544/8230804 by Witwatersrand University user on 14 October 2025

Briggs D. S., 1995, Am. Astron. Soc. Meeting, 187, 112.02
Brodwin M. et al., 2010, ApJ, 721, 90
Brunetti G., Blasi P., 2005, MNRAS, 363, 1173
Brunetti G., Jones T. W., 2014, Int. J. Mod. Phys. D, 23, 1430007
Brunetti G., Setti G., Feretti L., Giovannini G., 2001, MNRAS, 320, 365
Camilo F. et al., 2018, ApJ, 856, 180
Carilli C. L., Taylor G. B., 2002, ARA&A, 40, 319
Carlstrom J. E. et al., 2011, PASP, 123, 568
CASA Team, 2022, PASP, 134, 114501
Cassano R., Brunetti G., 2005, MNRAS, 357, 1313
Cassano R., Ettori S., Giacintucci S., Brunetti G., Markevitch M., Venturi T., Gitti M., 2010, ApJ, 721, L82
Cassano R. et al., 2013, ApJ, 777, 141
Cuciti V. et al., 2021, A&A, 647, A51
Cuciti V. et al., 2023, A&A, 680, A30
Dey A. et al., 2019, AJ, 157, 168
Dicker S. R. et al., 2020, ApJ, 902, 144
Di Gennaro G. et al., 2021, Nat. Astron., 5, 268
Di Gennaro G. et al., 2023, A&A, 675, A51
Di Gennaro G. et al., 2025, A&A, 695, A215
Di Mascolo L. et al., 2021, A&A, 650, A153
Dressler A., 1980, ApJ, 236, 351
Dressler A., Shectman S. A., 1988, AJ, 95, 985
Ensslin T. A., Biermann P. L., Klein U., Kohle S., 1998, A&A, 332, 395
Feretti L., Giovannini G., Govoni F., Murgia M., 2012, A&AR, 20, 54
Foley R. J. et al., 2011, ApJ, 731, 86
Fruscione A. et al., 2006, in Silva D. R., Doxsey R. E., eds, Proc. SPIE Conf. Vol. 6270, Observatory Operations: Strategies, Processes, and Systems. SPIE, Bellingham, p. 62701V
Gonzalez A. H. et al., 2015, ApJ, 812, L40
Gonzalez A. H. et al., 2019, ApJS, 240, 33
Graessle D. E., Evans I. N., Glotfelty K., He X. H., Evans J. D., Rots A. H., Fabbiano G., Brissenden R. J., 2007, Chandra News, 14, 33
Helfand D. J., White R. L., Becker R. H., 2015, ApJ, 801, 26
Heywood I., 2020, Astrophysics Source Code Library, record ascl:2009.003
Hilton M. et al., 2018, ApJS, 235, 20
Hilton M. et al., 2021, ApJS, 253, 3
Hlavacek-Larrondo J. et al., 2025, ApJ, 987, L40
Hoeft M., Brüggen M., 2007, MNRAS, 375, 77
Hugo B. V., Perkins S., Merry B., Mauch T., Smirnov O. M., 2022, in Ruiz J. E., Pierfedereci F., Teuben P., eds, ASP Conf. Ser. Vol. 532, Astronomical Data Analysis Software and Systems XXX. Astron. Soc. Pac., San Francisco, p. 541
Johnston S. et al., 2007, Publ. Astron. Soc. Aust., 24, 174
Jonas J., MeerKAT Team, 2016, Proc. Sci., MeerKAT Science: On the Pathway to the SKA (MeerKAT2016). SISSA, Trieste, PoS#001
Józsa G. I. G. et al., 2020, Astrophysics Source Code Library, record ascl:2006.014
Kale R., Botteon A., Eckert D., Santra R., Brunetti G., Venturi T., Cassano R., Dallacasa D., 2025, A&A, 698, A271
Kenyon J. S., Smirnov O. M., Grobler T. L., Perkins S. J., 2018, MNRAS, 478, 2399
Kim J., Jee M. J., Perlmutter S., Hayden B., Rubin D., Huang X., Aldering G., Ko J., 2019, ApJ, 887, 76
Knowles K. et al., 2021, MNRAS, 504, 1749
Krause E., Pierpaoli E., Dolag K., Borgani S., 2012, MNRAS, 419, 1766
Lindner R. R. et al., 2014, ApJ, 786, 49
Macario G. et al., 2013, A&A, 551, A141
McMullin J. P., Waters B., Schiebel D., Young W., Golap K., 2007, in Shaw R. A., Hill F., Bell D. J., eds, ASP Conf. Ser. Vol. 376, Astronomical Data Analysis Software and Systems XVI. Astron. Soc. Pac., San Francisco, p. 127
Mann A. W., Ebeling H., 2012, MNRAS, 420, 2120
Markevitch M., Vikhlinin A., 2007, Phys. Rep., 443, 1
Mauch T. et al., 2020, ApJ, 888, 61
Noordam J. E., Smirnov O. M., 2010, A&A, 524, A61
Norris R. P. et al., 2011, Publ. Astron. Soc. Aust., 28, 215
Offringa A. R. et al., 2014, MNRAS, 444, 606
Parekh V., van der Heyden K., Ferrari C., Angus G., Holwerda B., 2015, A&A, 575, A127
Parekh V. et al., 2020, MNRAS, 499, 404
Partridge B., López-Caniego M., Perley R. A., Stevens J., Butler B. J., Rocha G., Walter B., Zacchei A., 2016, ApJ, 821, 61
Petrosian V., Bykov A. M., 2008, Space Sci. Rev., 134, 207
Poole G. B., Babul A., McCarthy I. G., Fardal M. A., Bildfell C. J., Quinn T., Mahdavi A., 2007, MNRAS, 380, 437
Rajpurohit K. et al., 2020, A&A, 636, A30
Randall S. W., Markevitch M., Clowe D., Gonzalez A. H., Bradač M., 2008, ApJ, 679, 1173
Ruppin F. et al., 2020, ApJ, 893, 74
Sarazin C. L., 1988, X-ray Emission from Clusters of Galaxies. Cambridge Univ. Press, Cambridge
Sarazin C. L., 2002, in Feretti L., Gioia I. M., Giovannini G., eds, Merging Processes in Galaxy Clusters. Springer, Dordrecht, p. 1
Sarazin C. L., 2003, Phys. Plasmas, 10, 1992
Sarkar A. et al., 2024, ApJ, 962, 161
Savini F. et al., 2019, A&A, 622, A24
Sifón C. et al., 2016, MNRAS, 461, 248
Sikhosana S. P. et al., 2025, A&A, 698, L17
Smirnov O. M., 2011a, A&A, 527, A106
Smirnov O. M., 2011b, A&A, 527, A107
Smirnov O. M., 2011c, A&A, 527, A108
Smirnov O. M., 2011d, A&A, 531, A159
Smirnov O. M., Tasse C., 2015, MNRAS, 449, 2668
Staniszewski Z. et al., 2009, ApJ, 701, 32
Sunyaev R. A., Zeldovich Y. B., 1972, Comments Astrophys. Space Phys., 4, 173
Swetz D. S. et al., 2011, ApJS, 194, 41
Tasse C., 2014a, preprint (arXiv:1410.8706)
Tasse C., 2014b, A&A, 566, A127
Tasse C. et al., 2018, A&A, 611, A87
van Haarlem M. P. et al., 2013, A&A, 556, A2
van Weeren R. J. et al., 2017, Nat. Astron., 1, 0005
van Weeren R. J., de Gasperin F., Akamatsu H., Brüggen M., Feretti L., Kang H., Stroe A., Zandanel F., 2019, Space Sci. Rev., 215, 16
Véliz Astudillo S., Carrasco E. R., Nilo Castellón J. L., Zenteno A., Cuevas H., 2025, A&A, 693, A106
Wik D. R., Sarazin C. L., Ricker P. M., Randall S. W., 2008, ApJ, 680, 17
Yuan Z. S., Han J. L., 2020, MNRAS, 497, 5485
Yuan Z. S., Han J. L., Wen Z. L., 2022, MNRAS, 513, 3013

APPENDIX A: DECALS OPTICAL IMAGES

Downloaded from https://academic.oup.com/mnras/article/542/2/1544/8230804 by Witwatersrand University user on 14 October 2025

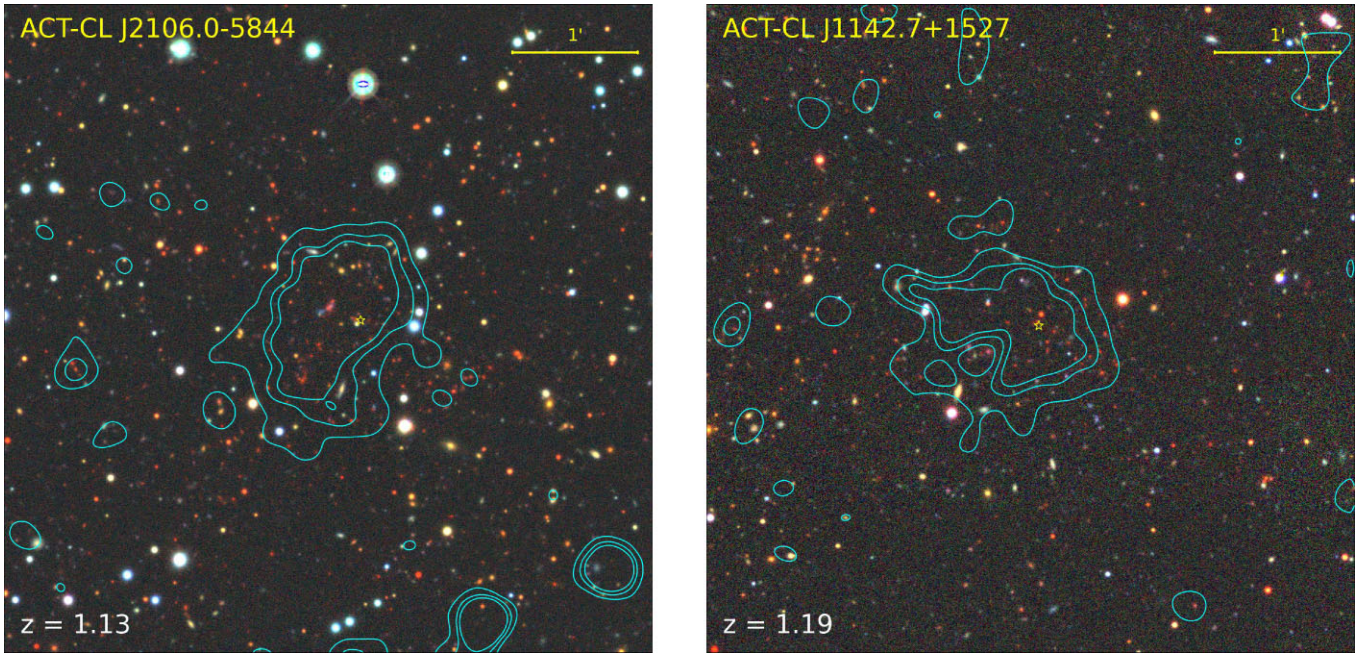

Figure A1. The optical *grz* images obtained from the DECaLS survey (Dey et al. 2019) are shown with MeerKAT *L*-band LR radio contours overlaid in cyan at levels of $\sigma_{\rm LR} \times [3, 6, 10]$. The yellow star indicates the position of the BCG, adopted from the ACT DR5 catalogue (Hilton et al. 2021). Left: ACT-CL J2106, with a 1σ noise level of 6.5 μJy beam^{-1}. Right: ACT-CL J1142, with a 1σ noise level of 7.2 μJy beam^{-1}.

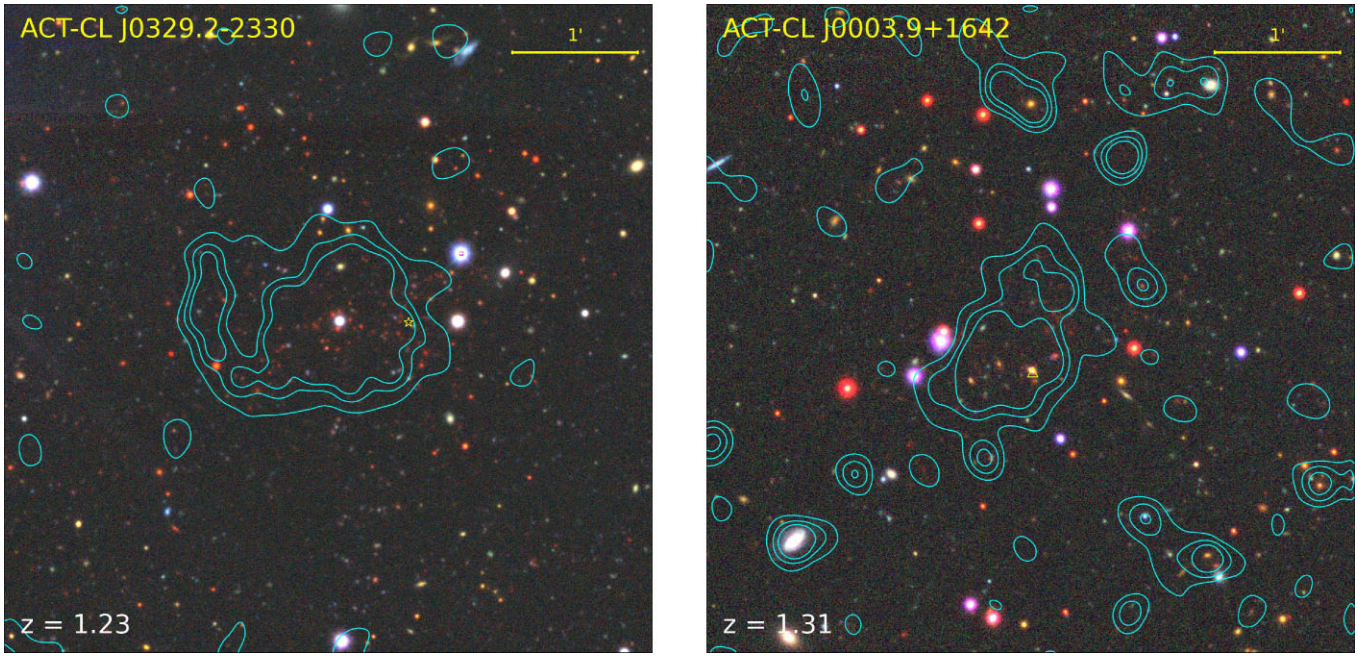

Figure A2. The optical *grz* images obtained from the DECaLS survey (Dey et al. 2019) are shown with MeerKAT *L*-band LR radio contours overlaid in cyan at levels of $\sigma_{\rm LR} \times [3, 6, 10]$. The yellow star/triangle indicates the position of the BCG, adopted from the ACT DR5 catalogue (Hilton et al. 2021). Left: ACT-CL J0329, with a 1σ noise level of 6.1 μJy beam^{-1}. Right: ACT-CL J0003, with a 1σ noise level of 9.2 μJy beam^{-1}.

Downloaded from https://academic.oup.com/mnras/article/542/2/1544/8230804 by Witwatersrand University user on 14 October 2025

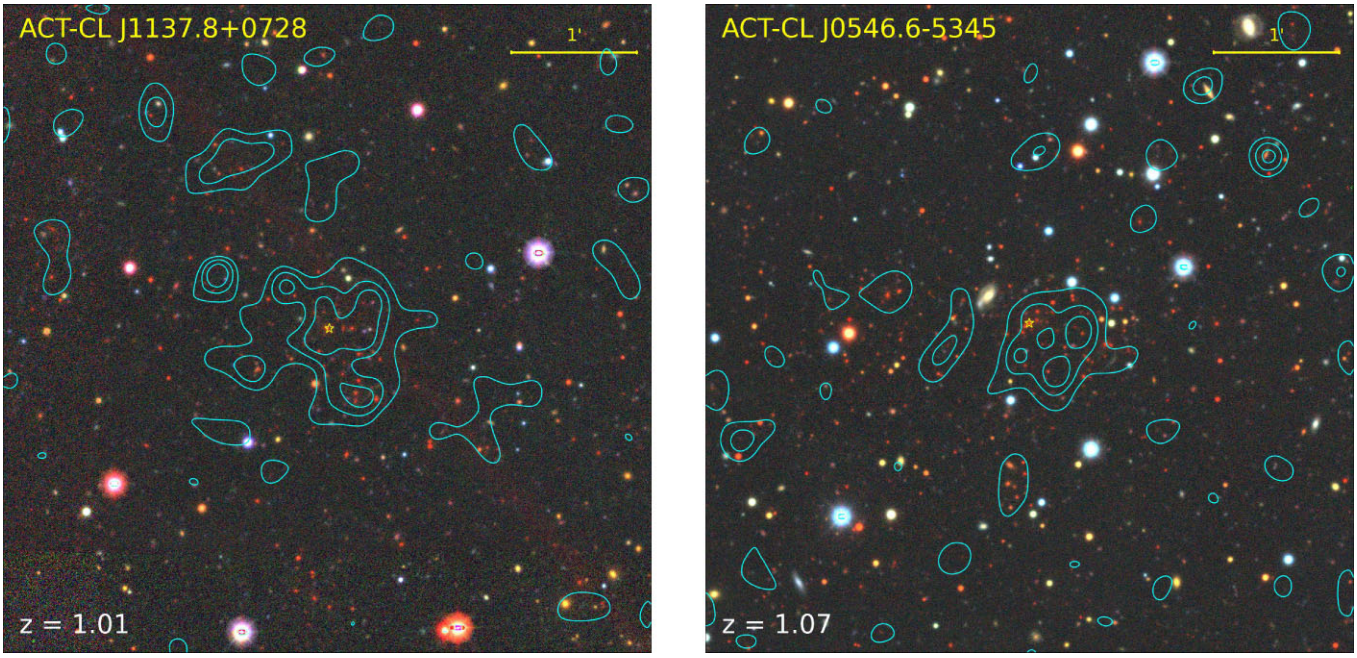

Figure A3. The optical *grz* images obtained from the DECaLS survey (Dey et al. 2019) are shown with MeerKAT *L*-band LR radio contours overlaid in cyan at levels of $\sigma_{\rm LR} \times [3, 6, 10]$. The yellow star indicates the position of the BCG, adopted from the ACT DR5 catalogue (Hilton et al. 2021). Left: ACT-CL J1137, with a 1σ noise level of 7.5 μJy beam^{-1}. Right: ACT-CL J0546, with a 1σ noise level of 9.4 μJy beam^{-1}.

APPENDIX B: HIGH- AND LOW-RESOLUTION IMAGES

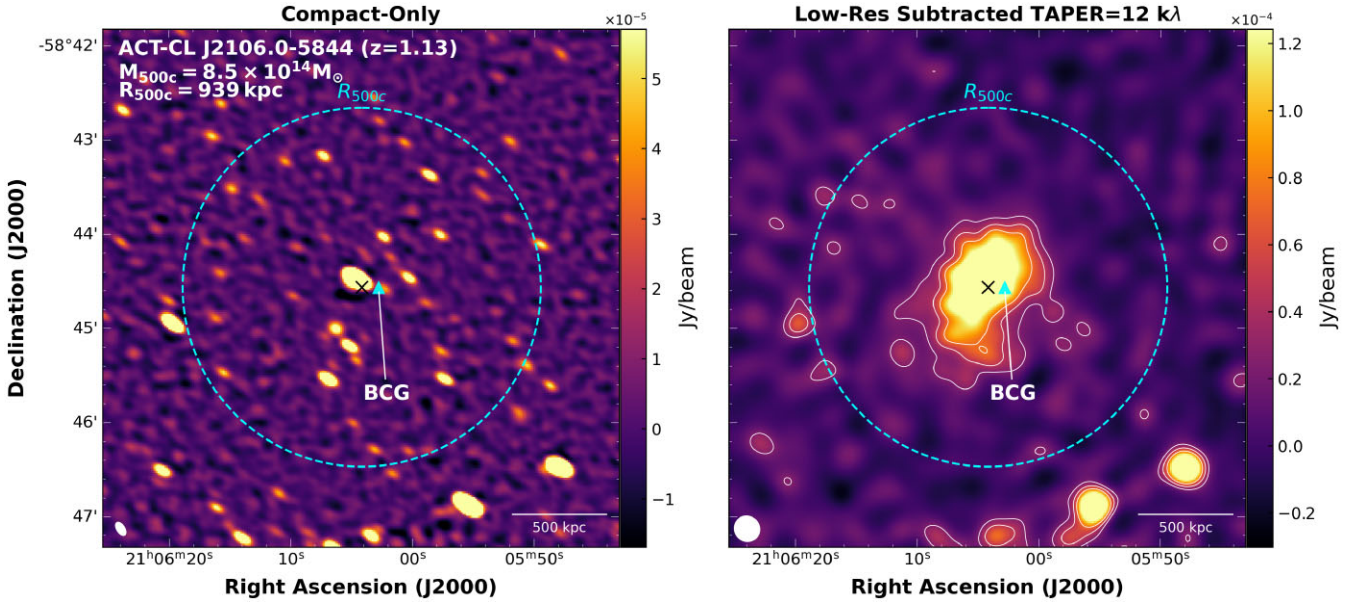

Figure B1. MeerKAT *L*-band radio images of ACT-CL J2106. The position of the BCG is indicated by a cyan triangle, while the black cross marks the location of the ACT SZ peak. Left: Compact-only image showing discrete radio sources. Right: LR, point-source subtracted image with white contours at levels of $\sigma_{\rm LR} \times [3, 6, 10]$; the 1σ noise level is 9.4 μJy beam^{-1}.

Downloaded from https://academic.oup.com/mnras/article/542/2/1544/8230804 by Witwatersrand University user on 14 October 2025

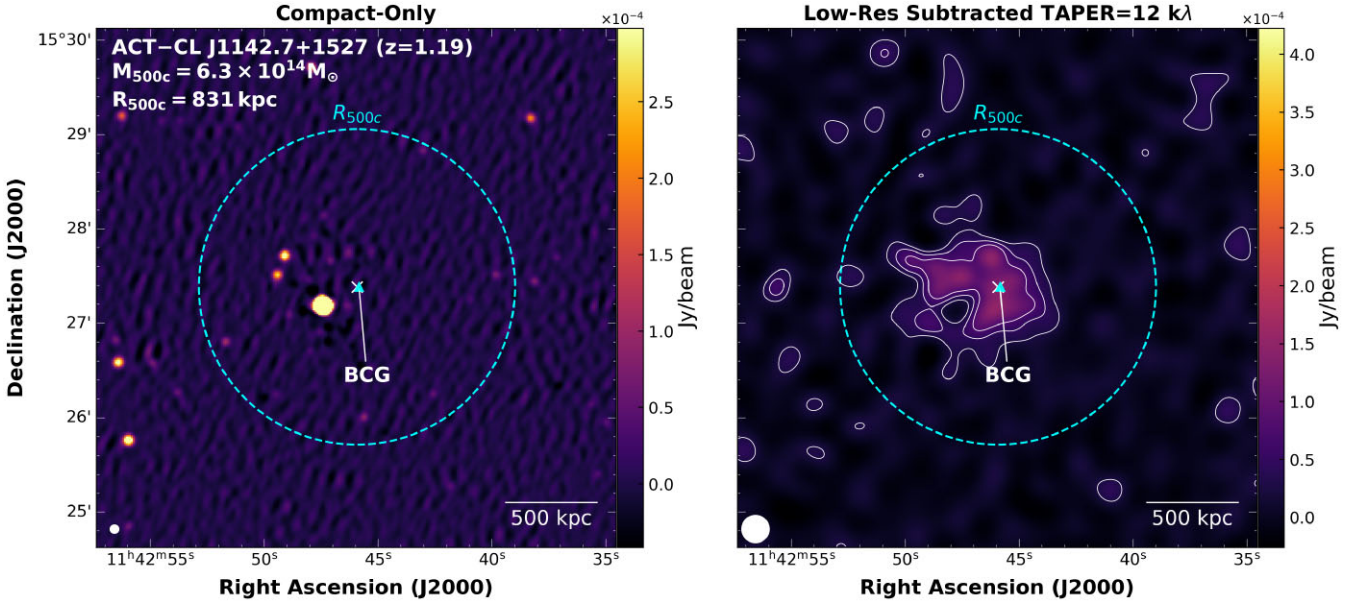

Figure B2. MeerKAT *L*-band radio images of ACT-CL J1142. The position of the BCG is indicated by a cyan triangle, while the black cross marks the location of the ACT SZ peak. Left: Compact-only image showing discrete radio sources. Right: LR, point-source subtracted image with white contours at levels of $\sigma_{\rm LR} \times [3, 6, 10]$; the 1σ noise level is 6.5 μJy beam^{-1}.

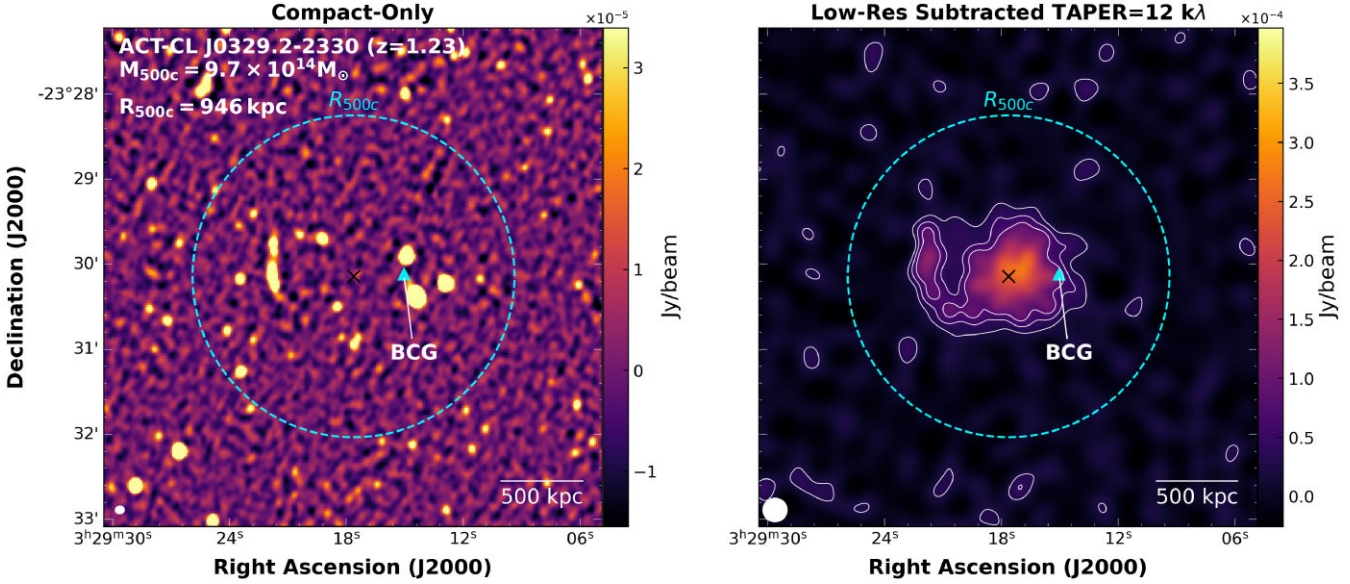

Figure B3. MeerKAT *L*-band radio images of ACT-CL J0329. The position of the BCG is indicated by a cyan triangle, while the black cross marks the location of the ACT SZ peak. Left: Compact-only image showing discrete radio sources. Right: LR, point-source subtracted image with white contours at levels of $\sigma_{\rm LR} \times [3, 6, 10]$; the 1σ noise level is 6.1 μJy beam^{-1}.

Downloaded from https://academic.oup.com/mnras/article/542/2/1544/8230804 by Witwatersrand University user on 14 October 2025

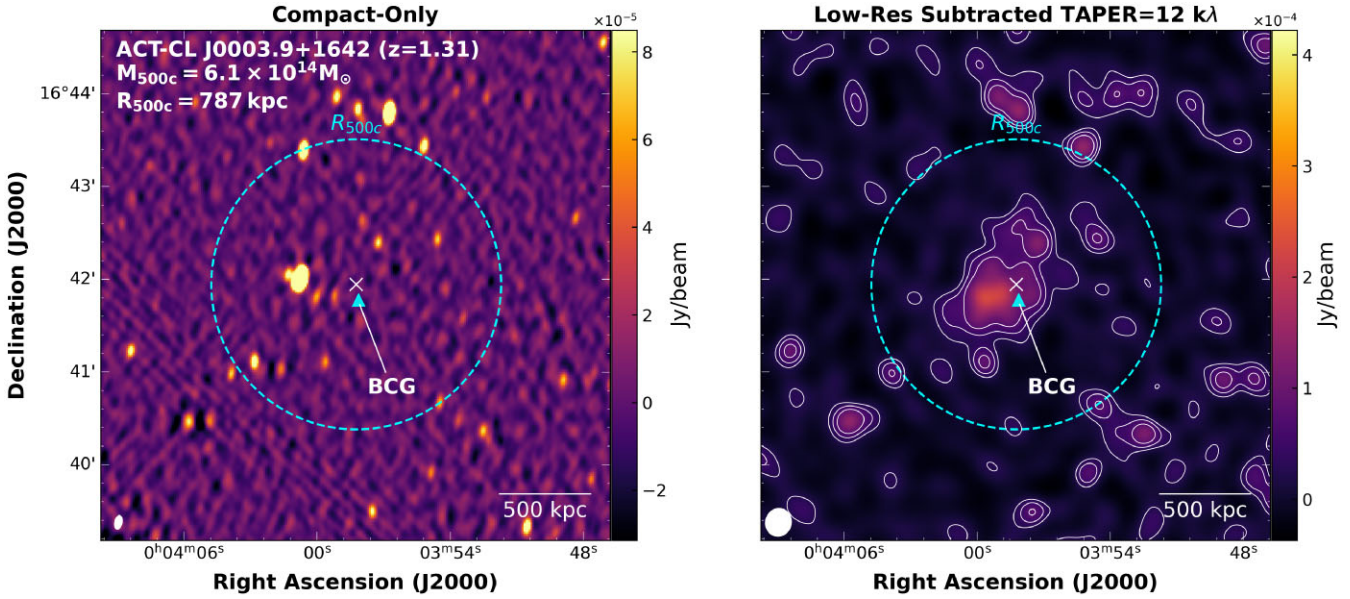

Figure B4. MeerKAT *L*-band radio images of ACT-CL J0003. The position of the BCG is indicated by a cyan triangle, while the black cross marks the location of the ACT SZ peak. Left: Compact-only image showing discrete radio sources. Right: LR, point-source subtracted image with white contours at levels of $\sigma_{LR} \times [3, 6, 10]$; the 1σ noise level is 9.2 μJy beam^{-1}.

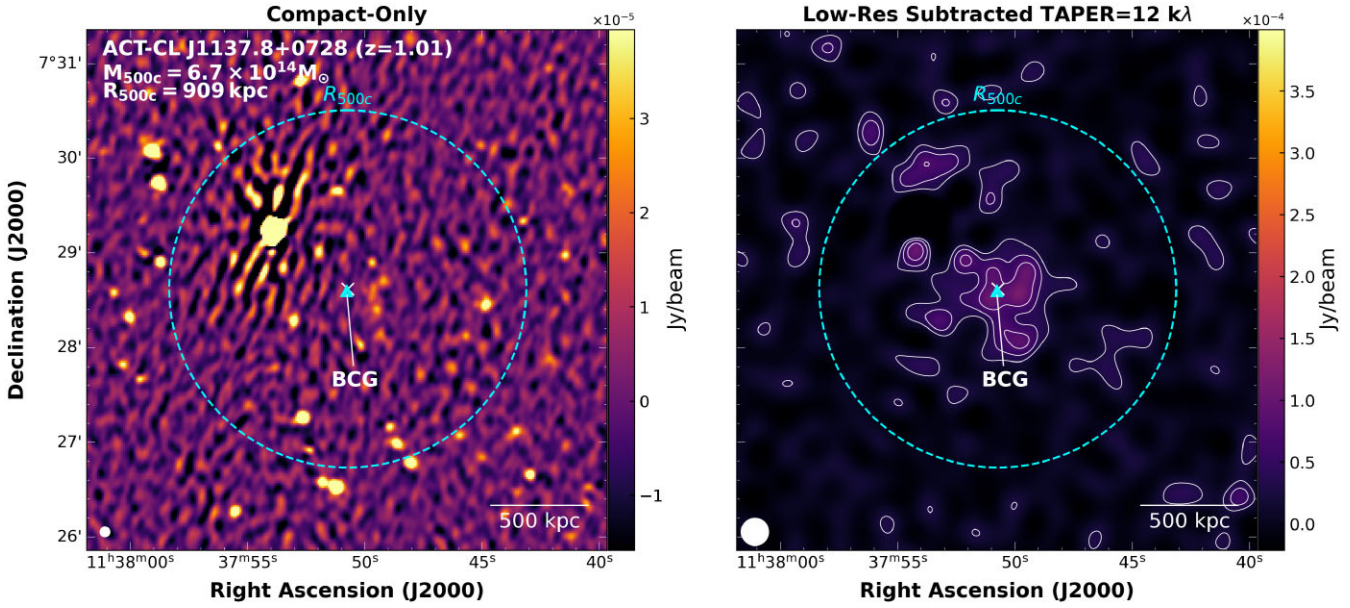

Figure B5. MeerKAT *L*-band radio images of ACT-CL J1137. The position of the BCG is indicated by a cyan triangle, while the black cross marks the location of the ACT SZ peak. Left: Compact-only image showing discrete radio sources. Right: LR, point-source subtracted image with white contours at levels of $\sigma_{LR} \times [3, 6, 10]$; the 1σ noise level is 7.5 μJy beam^{-1}.

Downloaded from https://academic.oup.com/mnras/article/542/2/1544/8230804 by Witwatersrand University user on 14 October 2025

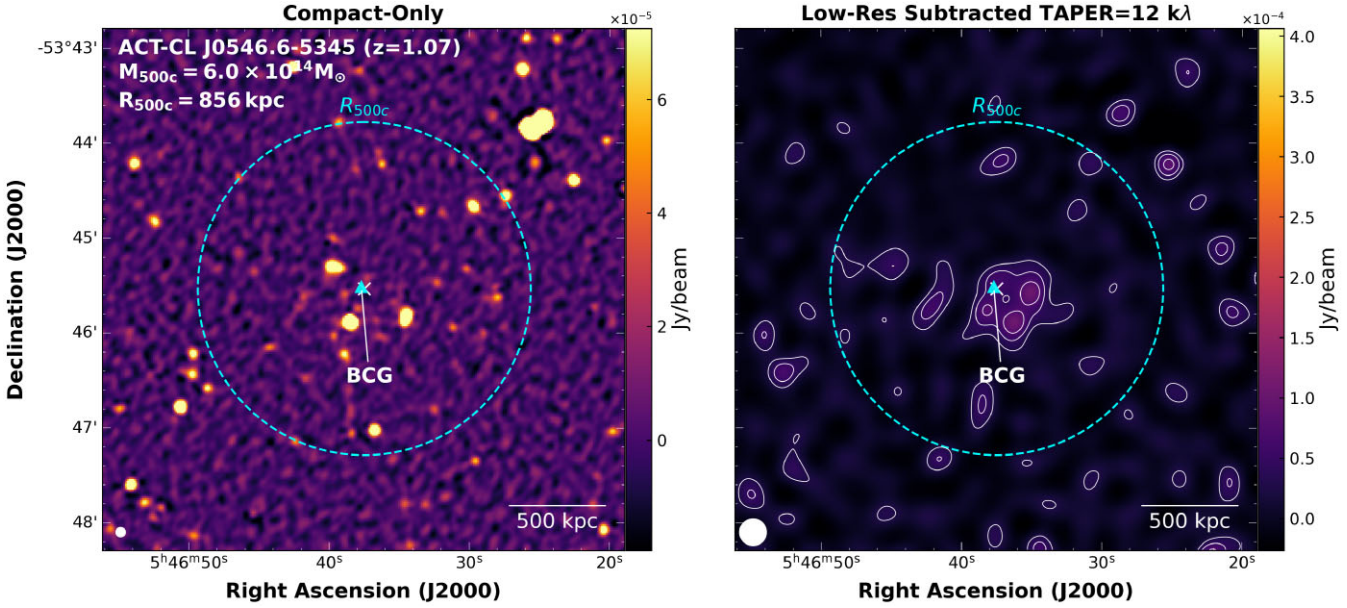

Figure B6. MeerKAT L-band radio images of ACT-CL J0546. The position of the BCG is indicated by a cyan triangle, while the black cross marks the location of the ACT SZ peak. Left: Compact-only image showing discrete radio sources. Right: LR, point-source subtracted image with white contours at levels of $\sigma_{\rm LR} \times [3, 6, 10]$; the 1σ noise level is 9.4 μJy beam^{-1}.

APPENDIX C: FITTING PROCEDURE AND PARAMETERS

We estimated the correlation parameters for radio haloes by fitting a power-law model to the $P_{1.4\,\rm GHz}$–M_{500} relation in log–log space, following the approach of Cassano et al. (2013). The fitting was performed using SCATTR, a regression tool that handles intrinsic scatter and uncertainties in both variables. The fitted relation is expressed as

$$\log\left(\frac{P_{1.4\,\rm GHz}}{10^{24.5}\,\rm W\,Hz^{-1}}\right) = B\log\left(\frac{M_{500}}{10^{14.9}\,\rm M_\odot}\right) + A, \qquad \text{(C1)}$$

where A is the intercept and B the slope. Our results give $B = 4.04 \pm 1.06$ and $A = -0.07 \pm 0.08$, which are notably steeper than those derived using BCES (Bivariate Correlated Errors and intrinsic Scatter) methods in previous studies (see Table C1).

Table C1. Fitting parameters from SCATTR, along with the parameters of the scaling relation from Cuciti et al. (2021) and Cassano et al. (2013).

Method	B	err(B)	A	err(A)
SCATTR	4.04	1.06	−0.07	0.08
BCES Y|X	2.96	0.50	0.01	0.10
BCES bisector	3.77	0.57	0.125	0.076

This paper has been typeset from a TEX/LATEX file prepared by the author.

Downloaded from https://academic.oup.com/mnras/article/542/2/1544/8230804 by Witwatersrand University user on 14 October 2025

© The Author(s) 2025.
Published by Oxford University Press on behalf of Royal Astronomical Society. This is an Open Access article distributed under the terms of the Creative Commons Attribution License (https://creativecommons.org/licenses/by/4.0/), which permits unrestricted reuse, distribution, and reproduction in any medium, provided the original work is properly cited.